Marine Cold-Air Outbreak Snowfall in the North Atlantic: A CloudSat Perspective

Marian E. Mateling[1*], Claire Pettersen[2], Mark S. Kulie[3], and Tristan S. L'Ecuyer[1]

[1] Department of Atmospheric and Oceanic Sciences, University of Wisconsin-Madison, Madison, WI, USA
[2] Climate and Space Sciences and Engineering, University of Michigan-Ann Arbor, Ann Arbor, MI, USA
[3] Advanced Satellite Products Branch, NOAA/NESDIS/Center for Satellite Applications and Research, Madison, WI, USA

[*] Corresponding author: Marian E. Mateling (mateling@wisc.edu)

Key Points:

- CloudSat observes that most snowfall (frequency and amount) in the North Atlantic is produced during marine cold air outbreaks (MCAOs)
- During MCAO conditions, CloudSat-derived cloud top heights deepen as reanalysis-derived low-level instability increases
- On average, snowing cloud top heights are shallow (< 3 km) during MCAOs while they are much deeper (> 3 km) during non-MCAO conditions

Abstract

This study analyzes the influence of marine cold-air outbreaks (MCAO) on snowfall and cloud properties in the North Atlantic Ocean using CloudSat observations. Comparing reanalysis-determined MCAO conditions (low-level instability) against "non-CAO" conditions, we find that MCAO conditions are associated with predominantly light snowfall rates (< 2 mm day^{-1} liquid water equivalent) whereas non-CAO conditions are more frequently associated with higher snowfall rates. Near cold-air sources, such as sea ice or cold continents, MCAO-forced snowfall rates tend to be more frequent and more intense. Additionally, 76% of snowing clouds identified during MCAO conditions are shallow (mean cloud top height < 3 km) stratocumulus, whereas 44% (43%) of clouds in non-CAO conditions are deeper nimbostratus (stratocumulus). With greater boundary layer instability (stronger MCAO conditions), CloudSat observes higher cloud top heights, reflecting a deepening boundary layer and the presence of two distinct cloud modes during MCAO conditions.

Plain Language Summary

The sudden intrusion of cold air over relatively warm open water is known as a marine cold-air outbreak and impacts the downstream weather and environment. This study analyzes snow and cloud observations from the CloudSat satellite during marine cold-air outbreak conditions in the North Atlantic Ocean. We find that most often snowfall in the North Atlantic is light, produced by shallow stratocumulus clouds, and is coincident with marine cold-air outbreaks. During non-cold-air outbreak conditions, most snowing clouds are deeper nimbostratus. This work identifies two cloud regimes present during marine cold-air outbreak conditions, distinguished by weaker snowfall rates and a decreased presence of stratocumulus clouds downstream from cold air sources.

1   Introduction

A marine cold-air outbreak (MCAO) is the advection of cold, dry air (originating over cold land or sea ice) over relatively warmer water, the interaction of which destabilizes the lower troposphere and can lead to convection, cloud formation, and precipitation (Brümmer, 1997; Brümmer, 1999; Renfrew & Moore, 1999). These events impact clouds, weather, ocean-atmosphere heat exchange, and deep ocean circulation at higher latitudes where in-situ observations are sparse (e.g., Dickson et al., 1996; Kolstad et al., 2009). MCAOs occur most frequently in the Northern Hemisphere, are generally longer meridionally than zonally, and tend to dissipate over the ocean as a function of air parcel distance (or "fetch") from the ice/land-water interface increases (Fletcher et al., 2016a). North Atlantic MCAOs are often found in the cold sector of cyclones (e.g., Kolstad et al., 2009; Fletcher et al., 2016a; Papritz & Grams, 2018; Afargan-Gerstman et al., 2020) and in association with polar lows which can cause severe weather (e.g., Shapiro et al., 1987; Kolstad et al., 2009; Abel et al., 2017; Landgren et al., 2019; Terpstra et al., 2021). On longer timescales, persistent anticyclonic blocking in the North Atlantic, that is found to inundate the Greenland Ice Sheet with precipitation (Papritz & Grams 2018; Pettersen et al., 2022), simultaneously forces cold air equatorward on its eastward flank,

initiating MCAOs impacting Europe (e.g., Papritz & Grams, 2018; Terpstra et al., 2021; Smith & Sheridan, 2021).

In the upstream region of MCAOs, turbulent heat fluxes force shallow roll convection that forms stratiform cloud "streets" (Hartmann et al., 1997; Brümmer, 1999). Strong sensible and latent heat fluxes deepen the boundary layer with increasing fetch, leading to taller cloud top heights downstream, a transition to open-cellular convective clouds (Brümmer, 1999; McCoy et al., 2017; Geerts et al., 2022), and enhanced precipitation rates (Brümmer, 1997; Abel et al., 2017). In order to identify MCAO conditions over water, studies generally use a steep lapse rate or potential temperature gradient threshold (e.g., Fletcher et al., 2016a; Fletcher et al., 2016b; West et al., 2019; Smith & Sheridan, 2020; Geerts et al., 2022) that would facilitate boundary layer convection to form clouds and precipitation. From a cloud perspective, the seasonality of high-latitude open cellular convective cloud regimes is positively correlated to the MCAO index (McCoy et al., 2017), such that most open cellular convection in the northern Atlantic is likely associated with an MCAO.

Globally, MCAOs are most frequent in the North Atlantic and the associated unique cloud regime can often be identified in visible satellite imagery (e.g., Brümmer, 1999; Renfrew & Moore, 1999; Abel et al., 2017; Terpstra et al., 2021; Sanchez et al., 2022; Geerts et al., 2022). More specifically, Fletcher et al. (2016a) identified that the highest frequency and strength (via lapse rate) of North Atlantic MCAOs occur along the Gulf Stream or western continental boundary, Labrador Sea, south of Greenland, and in the Norwegian Sea (Fletcher et al., 2016a). Some of these locations are proximal to sea ice and cold continental air, but others are preferential for MCAO occurrence due to warmer sea surface temperature (SST) associated with western boundary currents in the ocean (Fletcher et al., 2016a). Global climate models tend to underestimate stratiform cloud cover (Fletcher et al., 2016a, Geerts et al., 2022), and multi- and sub-grid-scale meteorological processes make MCAO clouds difficult to capture in models (known as the "grey zone" problem; Tomassini et al., 2017; de Roode et al., 2019). Several studies employ in-situ observations to resolve the finer-scale meteorological phenomena present during individual MCAO events (e.g., Brümmer, 1999; Renfrew & Moore, 1999; Geerts et al., 2022), though these observations may be limited in space and time.

The advent of satellite meteorology has evolved our understanding of MCAOs, as its unique cloud regime can often be identified in visible imagery (e.g., Brümmer, 1999; Renfrew & Moore, 1999; Abel et al., 2017; Terpstra et al., 2021; Sanchez et al., 2022; Geerts et al., 2022). Beyond the visible spectrum, clouds and precipitation in remote locations can now be observed via retrievals by CloudSat, a polar-orbiting satellite with a W-band radar onboard and measurement capabilities up to |82°| latitude (Stephens et al., 2002). CloudSat's highly-sensitive radar can detect even very light snowfall (Tanelli et al., 2008) and several CloudSat studies have documented frequent shallow convective snowfall over high-latitude oceanic regions (Battaglia & Delanoe, 2013; Wang et al., 2013; Kulie et al., 2016; Kulie & Milani, 2018; Battaglia & Panegrossi, 2020). Additionally, studies have shown that oceanic cumuliform snowfall production commonly occurs in the North Atlantic region and is intimately linked to sea ice coverage with a distinct seasonal cycle (Kulie et al., 2016; Kulie & Milani, 2018). These analyses surmise that MCAOs likely initiate this distinct shallow snowfall regime, but no direct connections were made by investigating associated environmental conditions.

In this work, we combine the 5th version of the European Centre for Medium-Range Weather Forecast's (ECMWF) Reanalysis, ERA5 (Hersbach et al., 2020) data products with CloudSat satellite snowfall and combined CloudSat-CALIPSO cloud retrievals to analyze the snowfall patterns and characteristics, as well as the cloud regimes present, during MCAOs over the North Atlantic Ocean. The use of snowfall only, and exclusion of mixed and liquid precipitation, provides key information on the presence and impact of MCAOs on the ubiquitous shallow snowfall observed by CloudSat. CloudSat snowfall estimates and cloud top height information from 2007-2010 are paired with an ERA5-derived MCAO flag to investigate how conditions vary between MCAO and "non-CAO" snowfall events and the seasonality of those variations. Section 2 presents our data and methodology for filtering data into MCAO and non-CAO categories. Section 3 illustrates results of this research. Section 4 further analyzes the meteorological conditions and CloudSat-derived characteristics of MCAO snowfall events over the Greenland and Barents Seas and discusses implications for how MCAOs are captured by satellite. Lastly, concluding remarks are provided in section 5.

2 Data & Methods

CloudSat is a polar-orbiting satellite that was launched in 2006 and is currently operational (Stephens et al., 2002; Stephens et al., 2008). Onboard is a near-nadir pointing W-band 94 GHz Cloud Profiling Radar (CPR; Im et al., 2005; Tanelli et al., 2008) that measures radar reflectivity and retrieves cloud and precipitation properties up to $|82°|$ latitude. The CPR footprint is single-beam at $1.8 \text{ km} \times 1.4 \text{ km}$ (along-track and cross-track, respectively) resolution. In 2011, a battery anomaly onboard the satellite resulted in a shift to daytime-only operations moving forward (Stephens et al., 2018). The loss of nighttime data was found to decrease global mean snowfall rate estimates by ~8% due to pronounced latitudinal sampling issues (Milani & Wood, 2021). For this study, we used data from January 2007 to December 2010 to avoid potential high-latitude seasonal biases from CPR daytime-only sampling deficiencies and allow for a more robust seasonal analysis.

CloudSat surface snowfall retrievals are from version R05 of the 2C-SNOW-PROFILE data product (Wood & L'Ecuyer, 2018) while cloud type and cloud-top heights (CTH) are from version R05 of the 2B-CLDCLASS-LIDAR data product (Sassen & Wang, 2008; Wang, 2019). Precipitation detected by the CPR is identified as snow if the entire atmospheric profile is below freezing, as determined in the 2C-PRECIP-COLUMN data product (more details in Haynes et al., 2009). If the phase determination is inconclusive in the 2C-PRECIP-COLUMN product, a secondary test in the 2C-SNOW-PROFILE product will flag precipitation as snow if the surface temperature is below freezing and the derived precipitation melt fraction at the surface is ≤0.1. If the precipitation melt level within the CPR profile is misidentified, however, this may lead to incorrect phase identification and consequently impact snowfall rate estimates (Shates et al. 2023). Snowfall rate is then derived in the 2C-SNOW-PROFILE product, an optimal estimation algorithm that uses CPR reflectivity alongside ancillary temperature and cloud mask data to identify a cloud layer producing snow. The CPR has a high (>85%) probability of detection of snowfall (Cao et al. 2014; Chen et al. 2016; Kodamana & Fletcher, 2021) and correctly assigns hydrometeors as frozen for 95% of snowfall events detected by surface observations (Kodamana & Fletcher, 2021). More specific details about the 2C-SNOW-PROFILE retrieval are available in

the Algorithm Theoretical Basis Document (ATBD; Wood & L'Ecuyer, 2018). The 2B-CLDCLASS-LIDAR product is an algorithm that uses CPR observations, lidar measurements by the Cloud-Aerosol Lidar and Infrared Pathfinder Satellite Observations (CALIOP) on the CALIPSO satellite (Winker et al., 2007), and observations from the Moderate Resolution Imaging Spectroradiometer (MODIS) instrument on the Aqua satellite (Wang, 2019). This combined active-passive product uses retrieved cloud properties (including CTH) in a decision tree to identify cloud types, such as cumulus, stratus, nimbostratus, stratocumulus, deep convective, etc. (Sassen & Wang, 2008). These satellites were part of NASA's A-Train orbit from 2007-2010, providing near-spatio-temporally matched CPR and CALIOP data for the 2B-CLDCLASS-LIDAR product. More specific details about the 2B-CLDCLASS-LIDAR product can be found in the ATBD (Wang, 2019).

Several caveats must be considered using CloudSat data products for this work. Relevant limitations of CPR retrievals include challenges in accurately modeling scattering effects, absorption by liquid water in the atmosphere, and that the highly-sensitive CPR signal gets attenuated at higher precipitation rates (> 1 mm h^{-1}; Liu 2008; Battaglia et al. 2008; Matrosov, 2007; Durden et al. 2010; Hiley et al. 2011; Cao et al. 2014, Norin et al. 2015; Chase et al. 2022). However, most oceanic snowfall rates detected by CloudSat are light (< 1 mm h^{-1}) and therefore less affected by attenuation (Matrosov, 2007; Hiley et al., 2011; Kulie et al., 2016). Additionally, the CPR is susceptible to ground-clutter contamination that can exceed 1 km over land surfaces (i.e., the radar "blind zone"), thus rendering near-surface CPR observations unreliable (Kulie & Bennartz, 2009; Durden et al., 2010; Bennartz et al., 2019; McIlhattan et al., 2017; McIlhattan et al., 2020; Shates et al. 2023). However, a reduced blind zone over ocean (~600 m; Maahn et al., 2014) lessens the uncertainty in using CloudSat data to examine *marine* cold-air outbreak (MCAO) conditions.

Notably, CALIOP is capable of detecting clouds below the CloudSat blind zone level (Winker et al., 2009; McErlich et al., 2021), but cannot resolve both low-level and optically thick clouds. This could lead to misidentification of cloud type and height (Mace et al. 2021), particularly of the unique, shallow cloud regimes associated with MCAOs (Yang & Geerts 2006; Geerts et al. 2022). Most clouds associated with MCAOs (both snowing and non-snowing) are of smaller scale than the CPR footprint (Gryschka et al., 2008; Wu & Ovchinnikov 2022) and so the 2C-SNOW-PROFILE snowfall retrieval may be impacted by the CPR not resolving small-scale snowing clouds. Regardless, overall uncertainty is reduced in the 2B-CLDCLASS-LIDAR product due to the combination of the CPR retrievals with that from the lidar (Wang 2019).

To determine the presence of MCAO conditions, we derived the sea-surface potential temperature (θ_{SST}) and potential temperature at 850 hPa (θ_{850}) using ERA5 temperature and pressure data. We define an MCAO where M $\equiv \theta_{SST} - \theta_{850} > 0$, as in Geerts et al. (2022), to identify regions of low-level instability (Papritz et al., 2015). In addition, we require that the ERA5 surface is flagged as ocean and contains no sea ice. The definition of the M index varies in literature using potential temperature at the 700, 800, or 850 hPa levels, but Fletcher et al. (2016a) determined that using 700 hPa potential temperature identified fewer high-latitude MCAOs while using the 850 hPa level (θ_{850}), produced similar results to 800 hPa potential temperature but identified more sub-tropical MCAO events. Positive M values that are relatively larger in magnitude (based on location) are referred to as "stronger" MCAOs and associated with

higher surface precipitation rates and taller cloud top heights (Geerts et al., 2022). During the COMBLE field campaign, Geerts et al. (2022), identified the 10th (90th) percentile of M values at a coastal Norwegian site as 1.3 K (7.1 K) with an average value of 4.1 K. The range of possible M values varies by region and varies between studies depending on the chosen definition of M. Based on the prior work by Fletcher et al. (2016a) and to remain consistent with Geerts et al. (2022), we used 850 hPa potential temperature to determine MCAO conditions.

Our region of interest is over open ocean surfaces in the North Atlantic (45° to 82° N, -76° to 40° E) where MCAO frequency is highest globally (Fletcher et al., 2016a). This window contains the region where the field campaign COMBLE (Cold-air Outbreaks in the Marine Boundary Layer Experiment) recently studied upstream meteorological conditions during MCAO events between Svalbard and Scandinavia (Geerts et al., 2022). For several decades, field campaigns have used aircraft measurements to study MCAOs in the Fram Strait and Norwegian Sea (Brümmer, 1992; Brümmer, 1996; Wendisch et al. 2019; Wendisch et al. 2022).

For non-spatial visualization of data (e.g., histograms), no gridding or interpolation is performed; each CloudSat retrieval is matched to a coincident ERA5 gridbox (0.25°). To map the data, we gridded the CloudSat data and interpolated ERA5 data products to 1° latitude × 2° longitude, a commonly-used resolution to analyze the CloudSat 2C-SNOW-PROFILE product at high-latitudes (e.g., Palerme et al., 2014; Parlerme et al., 2017; Souverijns et al., 2018). Per gridbox, we averaged across all CloudSat snowfall rate data, including zero values, to obtain a seasonal mean snowfall rate (absolute snowfall rate). To analyze the frequency of occurrence, however, we have removed zero snowfall rate values. CloudSat's orbit overlaps at high latitudes and is more spatially distributed at lower latitudes which may lead to low-sample biases or over-representation from a single event (Kulie et al. 2016; Milani & Wood 2021). For all gridded figures, gridboxes that contain fewer than 50 pixels of data (or footprints) over a season are not included to avoid these biases. Frequency of occurrence statistics are generated by normalizing each gridbox by the number of footprints. Regardless, gridding high-resolution satellite data runs the risk of smaller-scale cloud and precipitation features being potentially smoothed out. ERA5 data is gridded using nearest neighbor interpolation and then matched to the coincident CloudSat gridbox. For each CloudSat gridbox, we identify the median timestep and match this to the nearest-time ERA5 gridbox.

3   Results

The region of interest and seasonal frequency of occurrence of MCAO conditions (f_{MCAO}, defined as M>0) are plotted in Figure 1. As f_{MCAO} is derived from ERA5, it is plotted at 0.25° resolution. The ERA5 seasonal mean sea ice extent is outlined in pink (Fig. 1 b-e) and represents an average ≥50% coverage of a gridbox with sea ice. The red box encompasses the region where the COMBLE field campaign detected MCAOs (Geerts et al., 2022). Boreal winter (December, January, February; DJF) and transition seasons (March, April, May; MAM; September, October, November; SON) (Fig. 1a, b, d) show relatively frequent seasonal occurrence of MCAOs, with a general f_{MCAO}≥ 30%. Due to the infrequency of summertime (June, July, August; JJA) MCAOs (Fig. 1c, note the different color scale) and associated low snowfall rates (not shown), JJA is excluded from the remainder of this study.
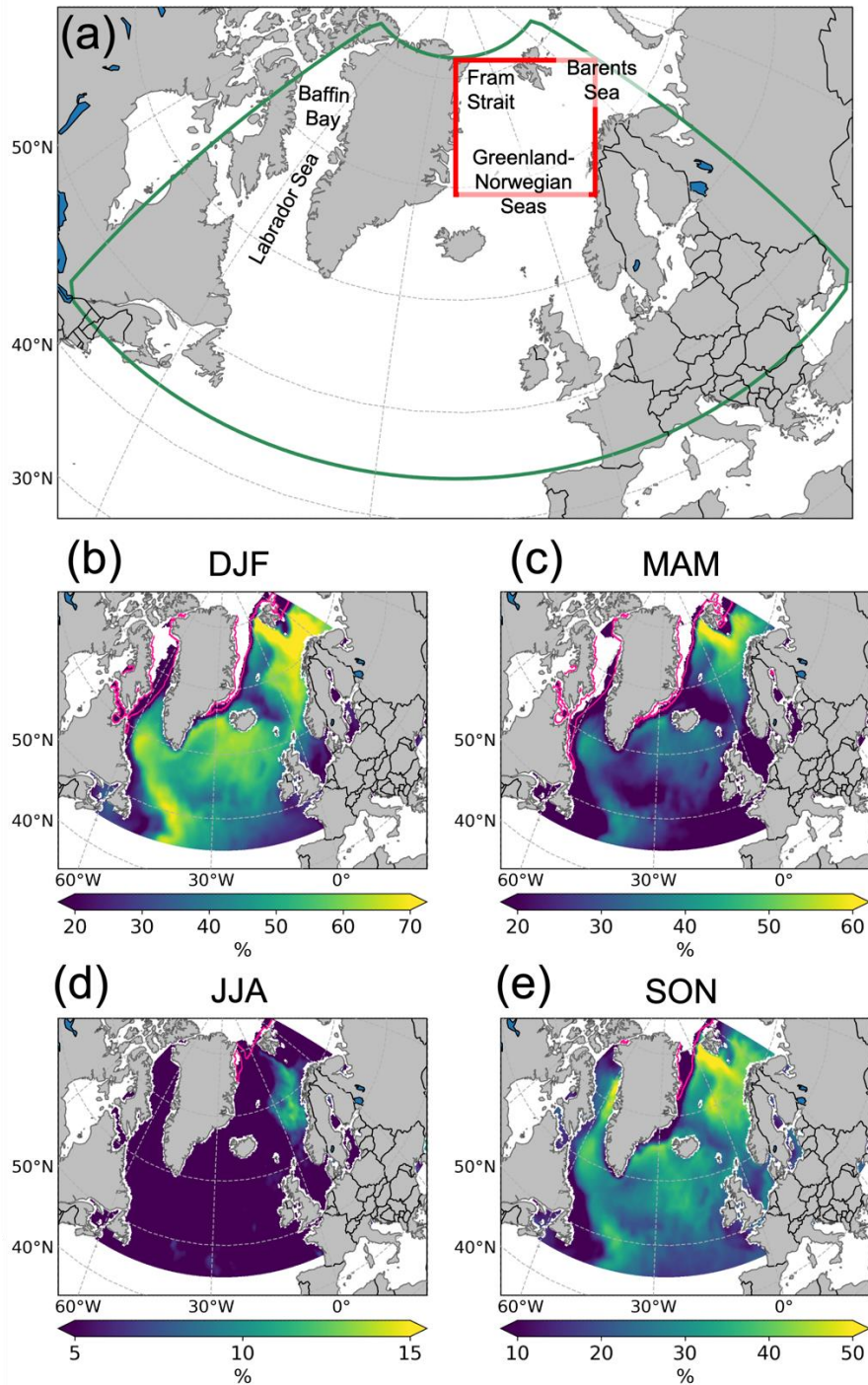
Fig. 1: (a) Region of study outlined in green with locations labeled. The approximate region where the COMBLE field campaign (Geerts et al. 2022) took place is outlined in red, near the north-easternmost corner of this window (60 to 82°N, -25 to 40°E). (b-e) Seasonal frequency of marine cold-air outbreak (MCAO) conditions in the North Atlantic determined using sea-surface potential temperature (θ_{SST}) and 850 hPa potential temperature (θ_{850}). MCAO conditions are defined where $\Delta\theta_{SST-850} > 0$. The pink contour represents an approximate seasonal mean sea ice extent ($\geq$50% sea ice concentration) from ERA5.

High f_{MCAO} values are found in regions consistent with Fletcher et al. (2016a): the Labrador Sea, the "North Atlantic" (parallel to western boundary currents and the Canadian coast), and the Norwegian Sea (which appears to include the Greenland Sea). Many other studies of North Atlantic MCAOs have identified high f_{MCAO} near Svalbard in the Greenland-Norwegian and/or Barents Seas (Brümmer, 1999; Kolstad et al., 2009; Afargan-Gerstman et al., 2020; Geerts et al., 2022), and the Labrador Sea (Renfrew & Moore, 1999; Kolstad et al., 2009; Smith & Sheridan, 2020; Terpstra et al., 2021). These same regions are also associated with frequent CloudSat-indicated shallow cumuliform snowfall maxima (Kulie et al., 2016; Kulie & Milani, 2018). In DJF (Fig. 1a), $f_{MCAO} > 60\%$ in the Labrador Sea, along the western boundary, and in the northeast in the Greenland-Norwegian and Barents Seas. In MAM (Fig. 1b), f_{MCAO} is largest (> 50%) in the Greenland-Norwegian Seas and a mean sea ice extent is at its furthest from the Arctic. Lastly, in SON (Fig. 1d) f_{MCAO} is highest (> 40%) in the Greenland-Norwegian Seas and in the Baffin Bay along Greenland's coast, where the mean sea ice extent has receded.

Figure 2 presents normalized (left) and raw count (right) histograms of CloudSat liquid water equivalent (LWE) snowfall (hereafter, "2CSNOW") rates during MCAO and non-CAO conditions in DJF (Fig. 2a, b), MAM (Fig. 2c, d), and SON (Fig. 2e, f). The distribution of 2CSNOW rates during MCAO conditions shows that the majority of snowfall events are light (< 0.1 mm h^{-1} LWE). For non-CAO conditions, the distribution 2CSNOW rates is broader with higher frequency of more intense snowfall rates (> 0.1 mm h^{-1}). Raw count histograms (Fig. 2b, d, f) also indicate that a majority of snowfall occurrences are produced during MCAO conditions across the spectrum and for all seasons, including more intense 2CSNOW rates. This indicates that CloudSat most often detects North Atlantic snowfall occurring during MCAO conditions, and therefore is most often detecting light snowfall (Fig. 2). The highest 2CSNOW rates as well as frequency occur in DJF which is reflected in the lower distributions of light 2CSNOW rates and higher distributions of larger rates (Fig. 2a, b). The remaining mapped plots are constrained by nonzero mean 2CSNOW rates and therefore share similar spatial coverage.
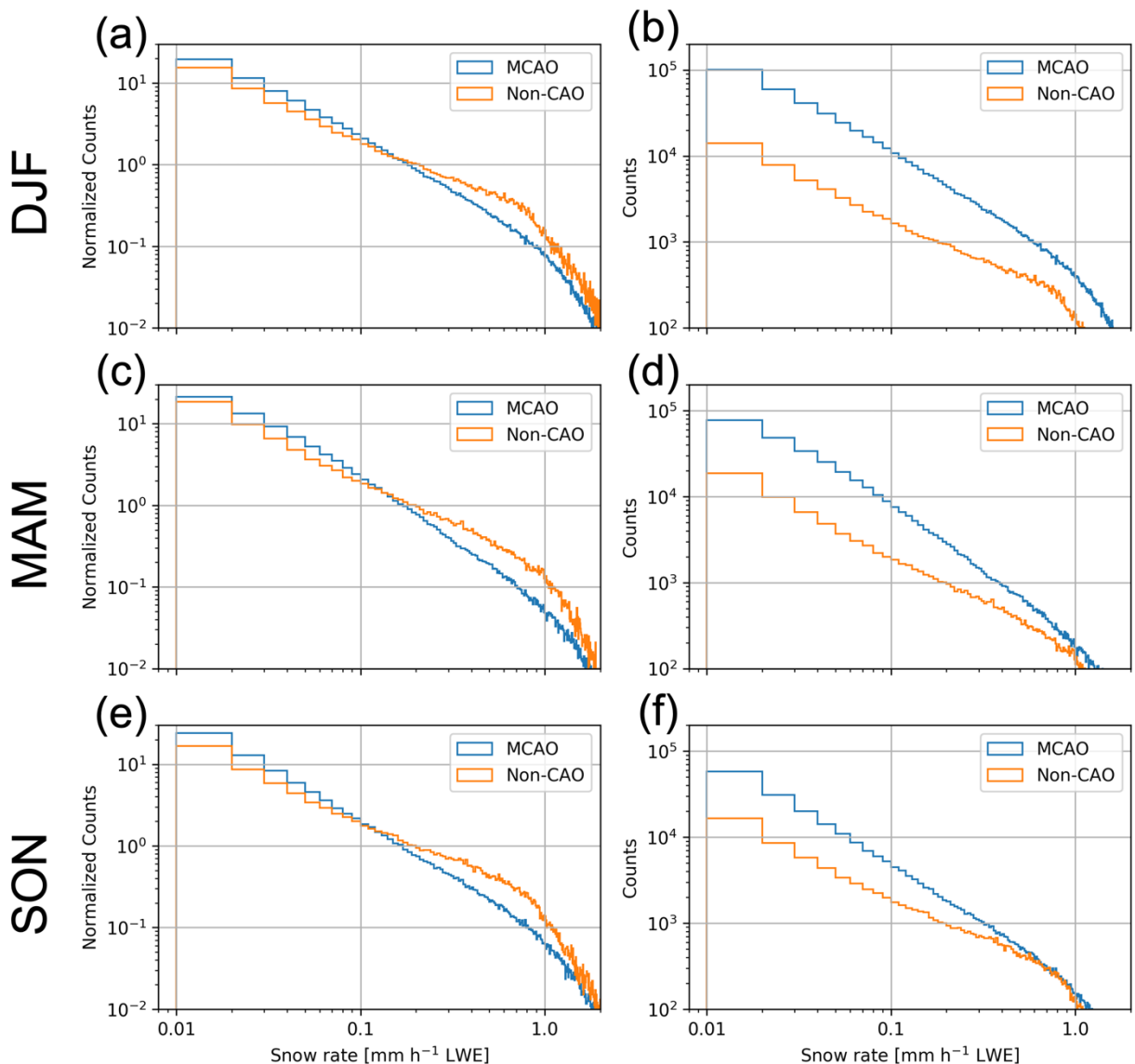
Fig. 2: Normalized (left) and raw count (right) histograms of seasonal surface snowfall rates ("2CSNOW") from CloudSat's 2C-SNOW-PROFILE data product from January 2007 to December 2010 in the North Atlantic. 2CSNOW rates are liquid water equivalent (LWE) and are categorized as occurring during MCAO (blue line) or non-CAO (orange line) conditions. MCAO occurrence is determined by spatio-temporally matching ERA5 data to each CloudSat pixel. Bin sizes are 0.01 mm h^{-1}.

To visualize the spatial distribution of North Atlantic snowfall, Figure 3 shows gridded seasonal mean 2CSNOW rates during MCAO (left column, Fig. 3a, c, e) and non-CAO (right column, Fig. 3b, d, f) conditions. CloudSat observes negligible snowfall in the southeast region of this window, regardless of MCAO conditions or season. The mean 2CSNOW rates exceed 0.05 mm h^{-1} LWE in regions where f_{MCAO} values are highest (Fig. 1). In DJF (Fig. 3a), this is in the Labrador Sea, along the western boundary, the Greenland-Norwegian Seas, and the Barents Sea. During non-CAO conditions (Fig. 3b), high rates are concentrated, generally along the mean sea

ice edge. During MAM CAO conditions (Fig. 3c), high 2CSNOW rates occur in the Labrador, Greenland-Norwegian, and Barents Seas. During non-CAO conditions (Fig. 3d), MAM 2CSNOW rates are generally lower than DJF (Fig. 3b), but are still highest along the sea ice edge. The 2CSNOW rates are lower in SON (Fig. 3e, f) than other seasons, but the highest of those rates are again coincident with high f_{MCAO} (Fig. 1d), in the Baffin Bay and Greenland-Norwegian Seas. SON during non-CAO conditions (Fig. 3f) is the least active season, as most snowfall occurs northward of 70°N and rates are generally < 0.05 mm h^{-1}. For all seasons, regardless of MCAO conditions, 2CSNOW rates eventually drop off in intensity in the downstream direction.
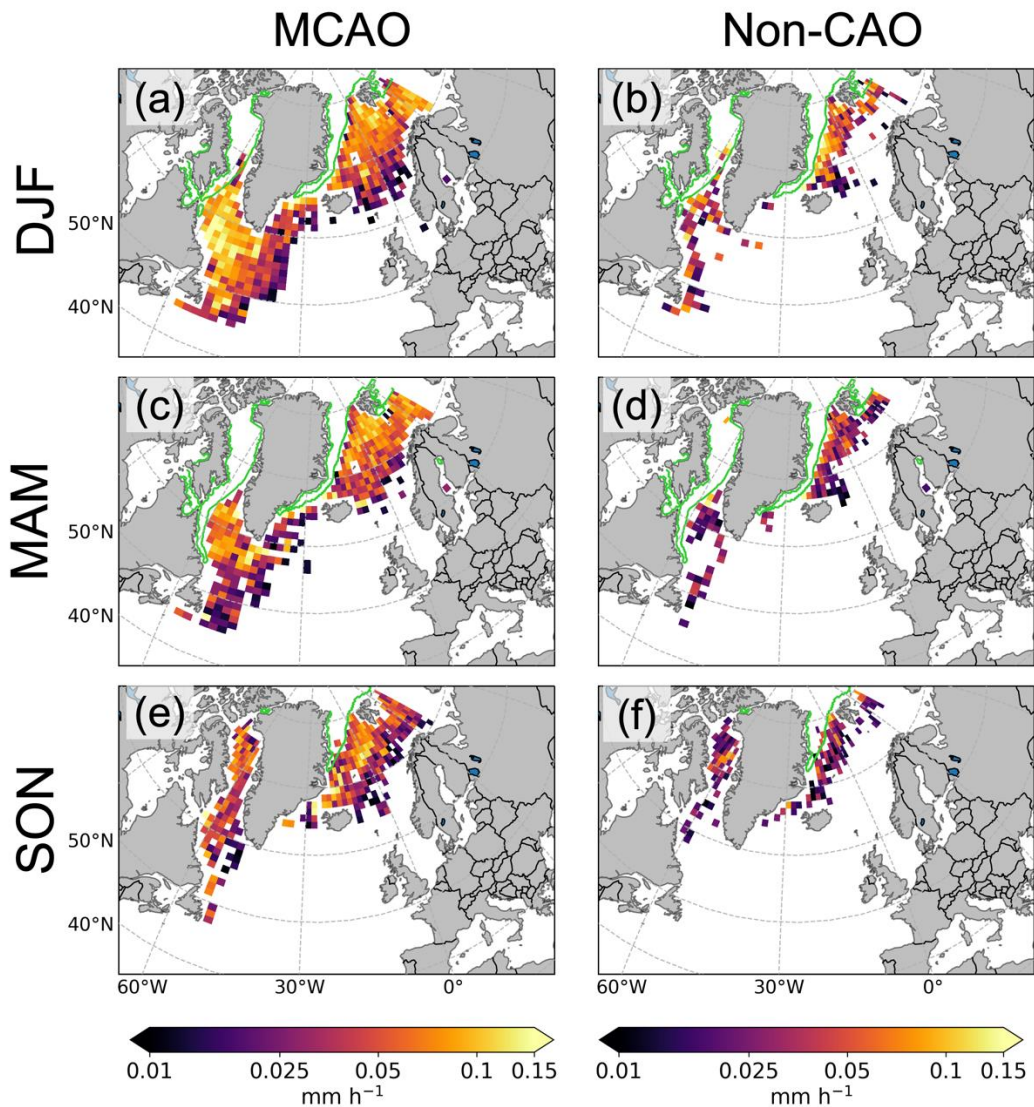

Fig. 3: Seasonal mean (Jan 2007 – Dec 2010) gridded CloudSat 2CSNOW rates during MCAO (left column) or non-CAO (right column) conditions. The green line indicates seasonal mean sea ice extent from the ERA5 dataset.

Figure 4 shows the conditional frequency of MCAO and non-CAO conditions constrained where the 2CSNOW rate ≥ 0.01 mm h^{-1} LWE ($f_{0.01}$; note the different colorbars for MCAO and non-CAO conditions). The $f_{0.01}$ during MCAO conditions in DJF (Fig. 4a) is highest ($> 9\%$) in the Labrador, Greenland-Norwegian, and Barents Seas. In MAM (Fig. 4c), $f_{0.01}$ values during MCAO conditions are smaller in the Labrador Sea, but $f_{0.01}$ is greater than DJF in the Fram Strait and Barents Sea MCAO pathways. In SON (Fig. 4e), MCAO $f_{0.01}$ maxima are located in Baffin Bay and the Greenland Sea, but $f_{0.01}$ magnitudes are greatly reduced compared to other seasons. Non-CAO $f_{0.01}$ values (Fig. 4b, d, f) are generally much lower than MCAO $f_{0.01}$ values, except along the mean sea ice edge and western boundaries. As was the case for the mean 2CSNOW rates shown in Figure 3, the spatial extent of $f_{0.01}$ is highest during DJF and lowest during SON. The $f_{0.01}$ during non-CAO conditions are even more spatially isolated. These results further highlight the dominance of snowfall events associated with MCAO conditions in the North Atlantic region.
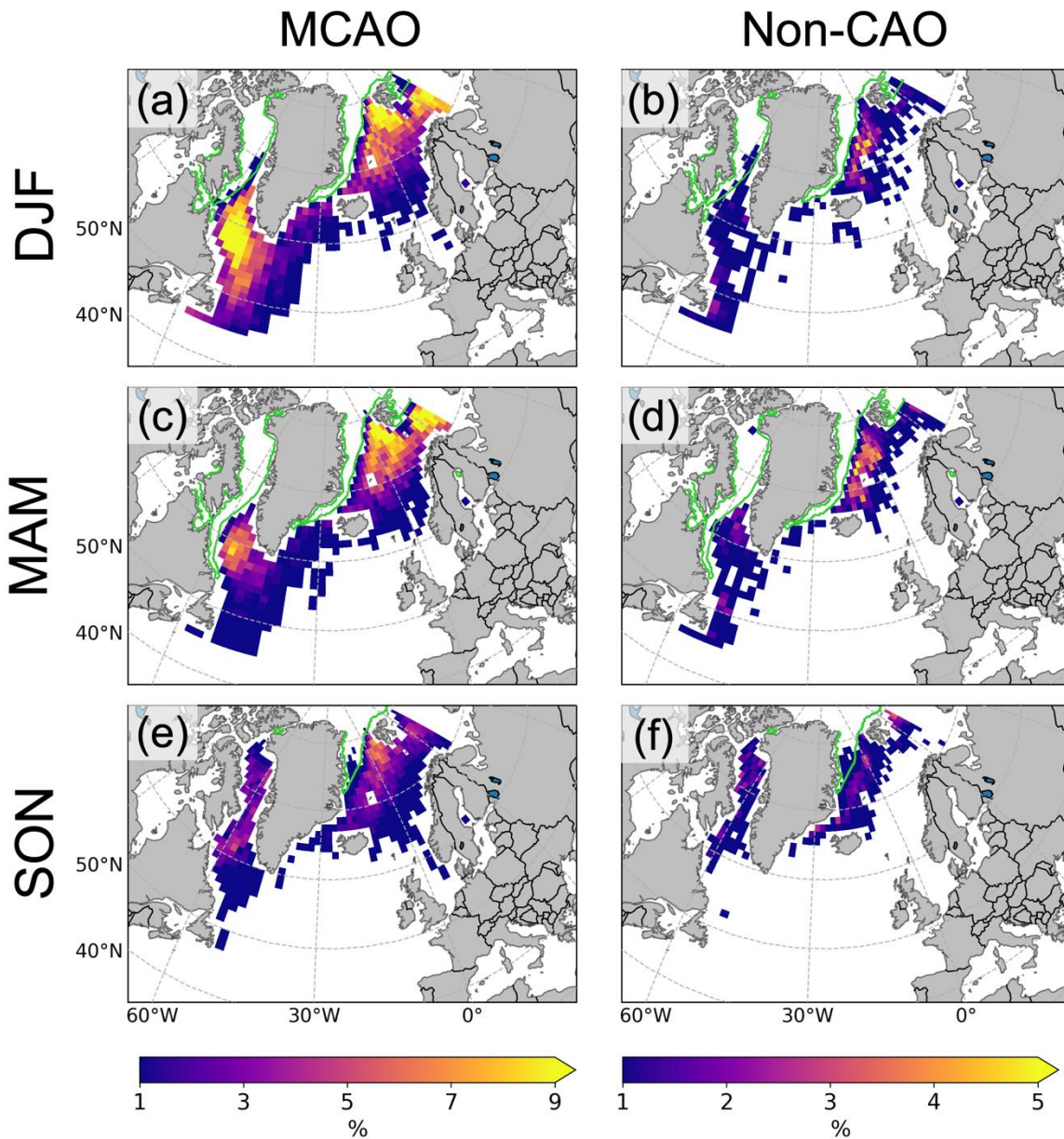
Fig. 4: Annual frequency of occurrence of gridded CloudSat snowfall rates exceeding or equal to 0.01 mm h^{-1} (LWE) during MCAO conditions (left column) and non-CAO conditions (right column). The green line indicates seasonal mean sea ice extent.

Further restricting to see how MCAO conditions impact more intense 2CSNOW rates, Figure 5 is the same as Figure 4, but for 2CSNOW rates ≥ 0.5 mm h^{-1} ("$f_{0.5}$"). This threshold represents a rate that exceeds the 90th percentiles for all seasons. At more intense 2CSNOW rates, $f_{0.5}$ magnitudes are more comparable between MCAO (Fig. 5a, c, e) and non-CAO (Fig. 5b, d, f) conditions and are therefore shown with the same scale. However, the locations of highest $f_{0.5}$ are strikingly similar to $f_{0.01}$ results (Figure 4). Generally, the intense 2CSNOW rates are more likely to occur in regions of high f_{MCAO} (Figure 1) or near sea ice during non-CAO conditions. Non-

CAO $f_{0.5}$ is less widespread geographically, indicating that more intense snow rates associated with non-CAO conditions are more isolated than for MCAO conditions.
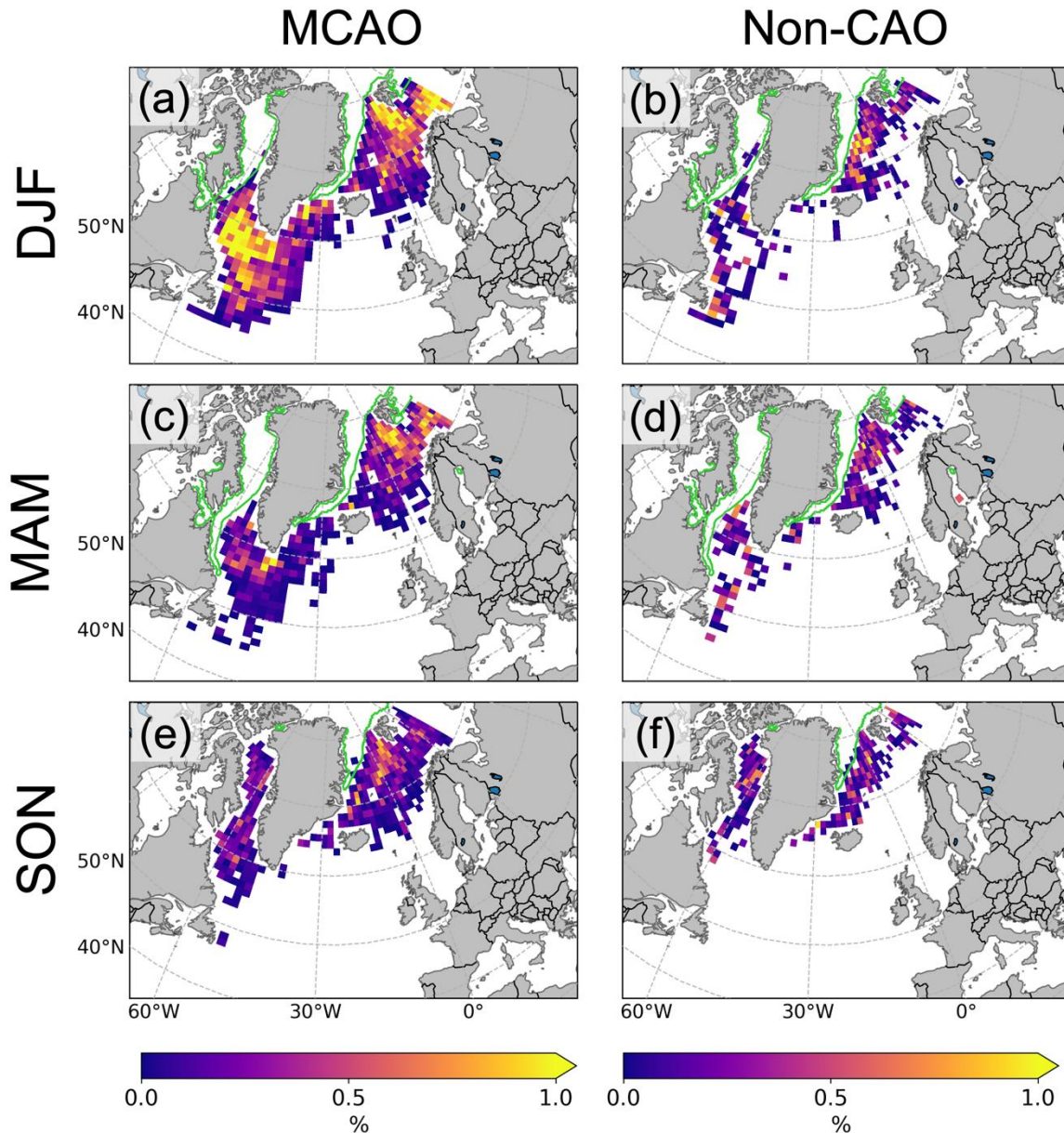

Fig. 5: Annual frequency of occurrence of gridded CloudSat snowfall rates exceeding or equal to 0.5 mm h^{-1} (LWE) during MCAO conditions (left column) and non-CAO conditions (right column). The green line indicates seasonal mean sea ice extent.

CloudSat-derived mean cloud-top heights (CTH) are shown in Figure 6 during snowfall (2CSNOW > 0 mm h^{-1}) under MCAO and non-CAO conditions. CTH are generally lower (taller) during MCAO (non-CAO) conditions with a spatiotemporal mean of 2.6 (4.0) km across all 3 seasons. Table 1 lists seasonal and combined (DJF, MAM, and SON) frequency of occurrence of cloud type, as defined by CloudSat's 2B-CLDCLASS-LIDAR product. The top row of Table 1

represents the frequency of occurrence across the entire basin for all 3 seasons, where snowing clouds are stratocumulus (Sc) 68.7% of the time, nimbostratus (Ns) 23.8% of the time, and 7.5% of snowing events are from other cloud types within the 2B-CLDCLASS-LIDAR designation (i.e., cumulus, stratus, cirrus, altostratus, etc.). During MCAO conditions, cloud occurrence is ~76% Sc (74-80% inter-seasonally), with the max occurrence in MAM (79%). Ns clouds make up ~18% of snowing MCAO clouds (15-20% inter-seasonally), with the max occurrence in DJF (19.8%). Non-CAO conditions have comparable frequency of Sc (44%) and Ns (43%) clouds for all seasons (respectively, 40-45% and 38-46% inter-seasonally), meaning that Ns clouds are more frequent and Sc less frequent during non-CAO conditions.
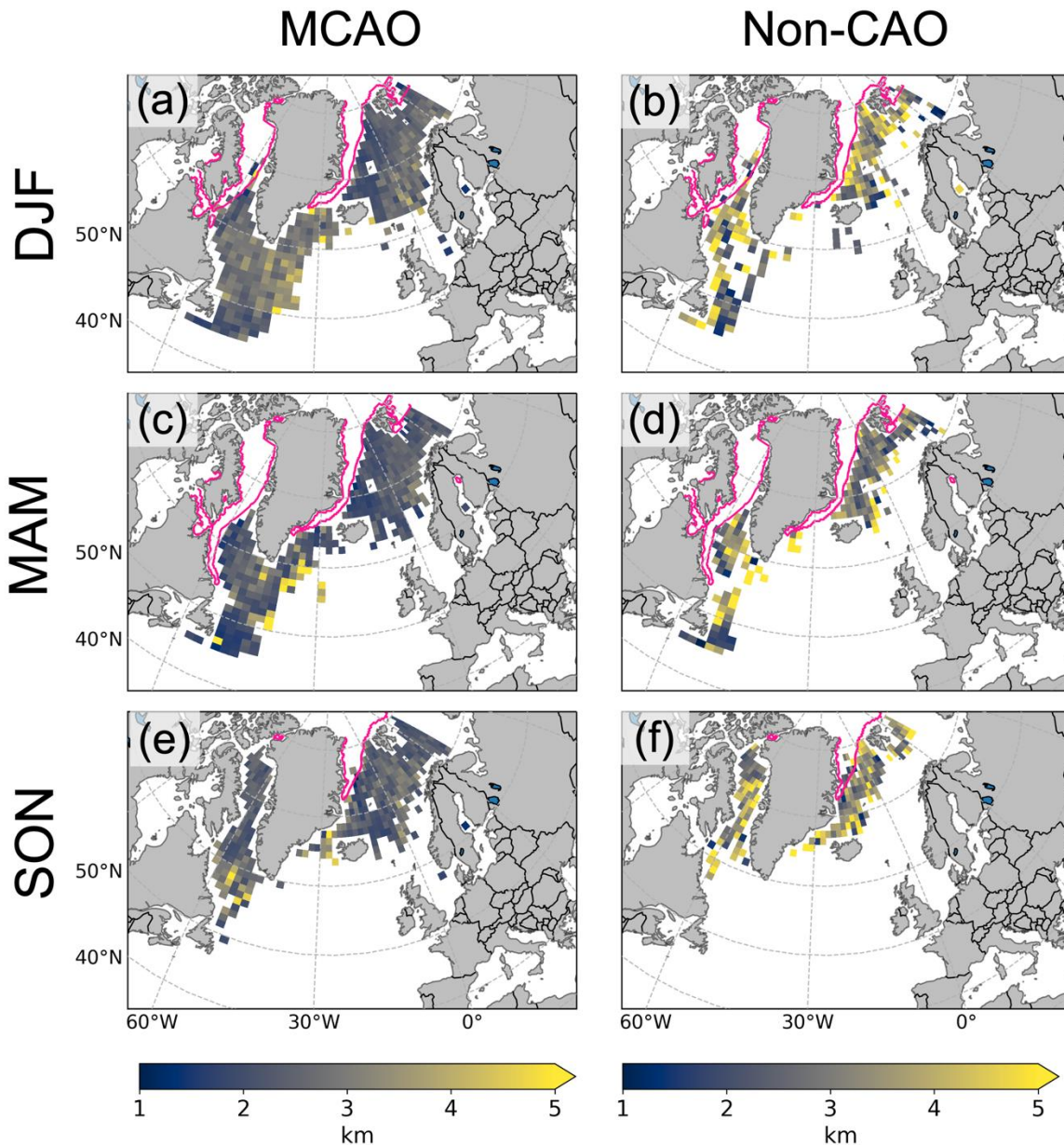
Fig. 6: Seasonal mean cloud-top height (CTH) derived from CloudSat's 2B-CLDCLASS-LIDAR during MCAO conditions (left column) and non-CAO conditions (right column). The pink line indicates seasonal mean sea ice extent.

Frequency of occurrence [%]		Stratocumulus	Nimbostratus	Other
Combined seasons MCAO + Non-CAO		68.7	23.8	7.50
Combined seasons (DJF + MAM + SON)	MCAO	75.6	18.4	6.00
	Non-CAO	44.0	43.1	12.9
DJF	MCAO	74.5	19.8	5.70
	Non-CAO	45.2	44.8	10.0
MAM	MCAO	79.0	15.5	5.50
	Non-CAO	46.6	38.9	14.5
SON	MCAO	73.9	19.1	7.00
	Non-CAO	40.6	46.6	12.8

Table 1: Seasonal and combined (DJF, MAM, and SON) frequency of occurrence of cloud type derived from CloudSat's 2B-CLDCLASS-LIDAR during snowing MCAO and non-CAO conditions.

In Figure 7, 2D histograms of ERA5 2-meter temperature (T2M) and total column water vapor (TCWV) exhibit the seasonal environmental conditions in which CloudSat detects snowfall. There appears to be distinct relationships between TCWV and T2M for snowfall during MCAOs (Fig. 7a, c, e) versus during non-CAO (Fig. 7b, d, f) conditions, with little seasonal variation. Generally, MCAO snowfall observed by CloudSat is coincident with T2M between 260 to 280 K and TCWV between 2 to 10 mm. While there are far fewer instances of CloudSat snowfall coincident with non-CAO conditions, it mostly occurs at warmer T2M (270-280 K) and moister TCWV (5-15 mm). Unsurprisingly, snowfall retrieved during MCAOs often occurs during colder (T2M < 265 K) and drier conditions (TCWV < 5 mm) than observed for non-CAO conditions. Non-CAO conditions, on the other hand, frequently produce snowfall in a moister environment (TCWV > 10 mm) but not necessarily warmer, as the snow will melt at higher near-surface temperatures indicated here by higher T2M. Snowfall occurrence when T2M > 283 K may be due to one of more of the following: (a) the 2C-SNOW-PROFILE using surface temperature data from the ECMWF forecast model, (b) differences in spatio-temporal resolution between CloudSat and ERA5 data, and (c) deficiencies in CPR retrievals of precipitation and phase, addressed in Section 2. The higher TCWV during non-CAO conditions is consistent with higher snowfall rates observed along the seasonal mean sea ice extent east of Greenland in Fig. 2b, d, f.
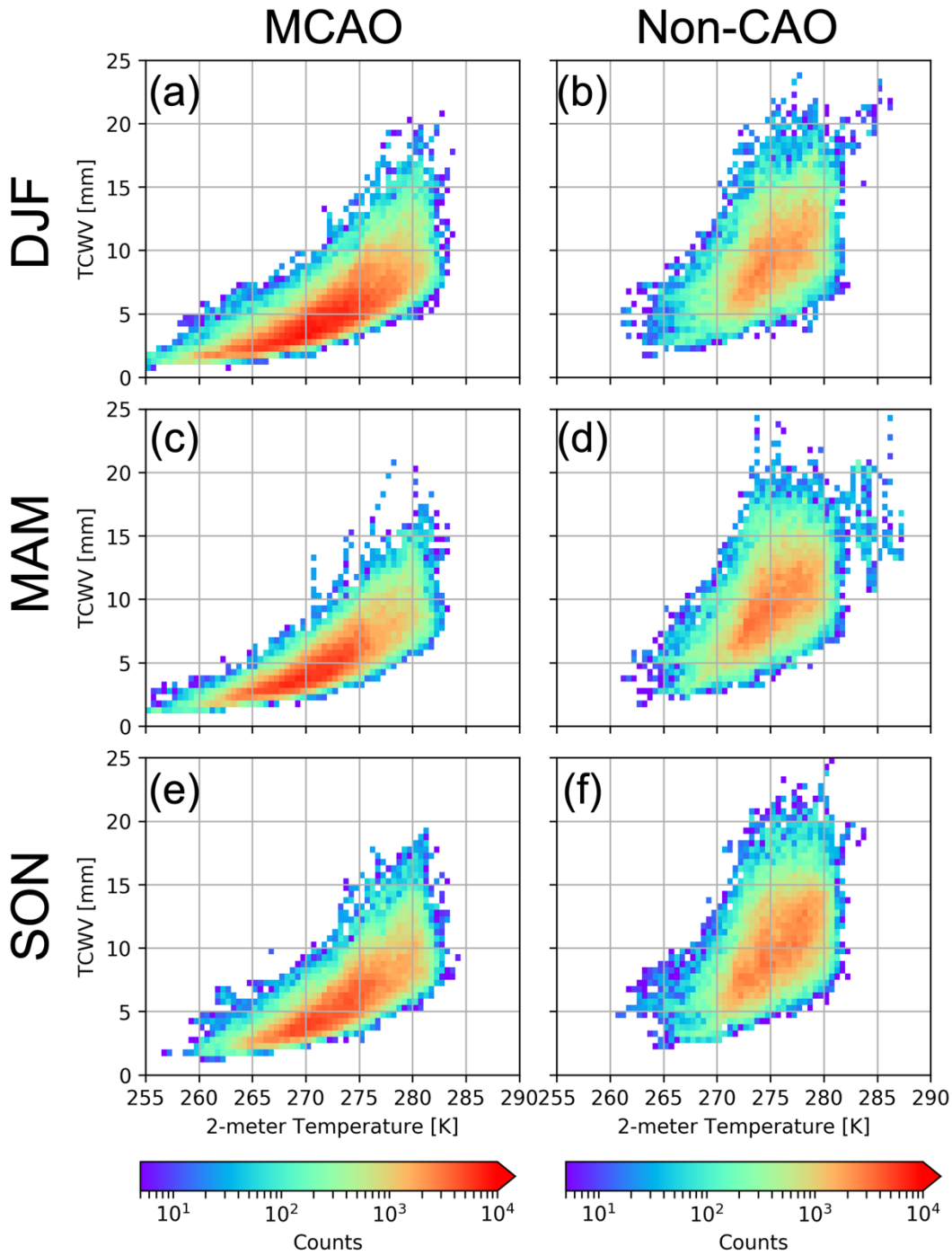
Fig. 7: Histograms of ERA5 2-meter temperature (T2M) and total column water vapor (TCWV) during snowing (2CSNOW > 0) MCAO conditions (left column) and non-CAO conditions (right column).

4 Discussion

The high f_{MCAO} identified along western continental and sea ice boundaries as well as in the Labrador, Greenland-Norwegian, and Barents Seas (Figure 1) align with findings in previous ground-based or model-based studies of MCAOs (e.g., Kolstad et al., 2009; Fletcher et al., 2016a; Papritz & Spengler 2017; Afargan-Gerstman et al., 2020). Upon initial investigation, we found that most of the CloudSat snowfall in the North Atlantic is light (<0.1 mm h^{-1}; Fig. 2) and most occurrence is coincident with MCAO conditions (Figures 2 and 4), regardless of season and including the most intense snowfall rates ($\geq$ 0.5 mm h^{-1}; Fig. 5). Spatially, the regions with the highest seasonal mean snowfall rates from CloudSat also coincide with regions of frequent MCAO occurrence (Figure 3). Higher mean snowfall rates may be attributed to the association of North Atlantic MCAO occurrence and midlatitude storm tracks (Papritz & Spengler, 2017; Papritz & Grams, 2018), cold sectors of cyclones (Kolstad et al., 2009; Fletcher et al., 2016a), and polar lows (Rasmussen and Turner 2003; Terpstra et al., 2021). Persistent anticyclonic blocking over the Greenland Ice Sheet (e.g., Hanna et al. 2016) and in the North Atlantic (e.g., Papritz & Grams, 2018) may promote MCAO formation east of Greenland as air masses on the eastern flank originate from cold continental or sea ice locations and advect over the open ocean. West of Greenland, this circulation advects warm, moist air onto the Greenland Ice Sheet and is responsible for the majority of enhanced SON snowfall events over central Greenland (Pettersen et al., 2022). This warm air would be categorized as non-CAO over the Baffin Bay if $\theta_{SST} \leq \theta_{850}$, which may explain enhanced SON 2CSNOW rates west of Greenland during non-CAO conditions (Fig. 3f). Additionally, enhanced mean snowfall rates and frequency along the sea ice edge during non-CAO conditions (Fig. 3-5) may be driven by warm-air intrusions that are common in this region (Woods et al., 2017), comparably low sampling of non-CAO conditions, or a combination of the two.

On average, snowing CTHs are much lower during MCAO conditions (< 3 km), and though less frequent, snow during non-CAO conditions is predominately produced by taller clouds (> 3 km; Fig. 6). In the Labrador Sea, mean CTH can exceed 3 km in some gridboxes during MCAO conditions, suggesting vigorous convective snow coincident with where the mean snow rates are high (Fig. 3), presence of tall nimbostratus clouds (Table 1), or a combination of the two. From a seasonal perspective, DJF is the most active in terms of snowfall rates, spatial extent of MCAO-coincident snowfall ($f_{0.01}$) including intense snowfall ($f_{0.5}$), and f_{MCAO}, followed by MAM and then SON. The mean sea ice coverage is greatest during MAM, which can both provide cold air but also inhibits surface heat fluxes and convection (Geerts et al., 2022). The lower sea ice extent in DJF likely plays a role in it being the most active MCAO season. Kulie & Milani (2018) identified similar spatial and seasonal patterns of shallow cumuliform (cumulus and Sc) snowfall in the CloudSat dataset with respect to sea ice extent, finding that limited surface heat fluxes and convection over sea ice strongly decrease snowfall production from shallow Sc and cumulus clouds.

Our results in Table 1 show that the dominant snowing cloud types in this basin are stratocumulus (~69%) and nimbostratus (~24%), aligning with previous findings in Kulie et al. (2016) that cumulus and Sc clouds account for >60% of oceanic snowfall events in the 2B-CLDCLASS CloudSat product (different than the 2B-CLDCLASS-LIDAR product used here). Kulie et al. (2016) used 2B-CLDCLASS cloud type to partition CloudSat observations with the assumption that shallow cumuliform snowfall events are largely forced by MCAO conditions. Table 1 indicates a vast majority (76%) of MCAO snow occurrences are indeed Sc (though in

our study, cumulus is grouped into the "other" category). However, 18% of snowing clouds during MCAO conditions are Ns, calling into question the assumption that this cloud type does not contribute much to MCAO snowfall amounts made in Kulie et al. (2016) and Kulie & Milani (2018). Unlike the CPR-only 2B-CLDCLASS product used in those studies, the 2B-CLDCLASS-LIDAR contains collocated CPR with CALIOP measurements. The lidar is more sensitive to mid- to high-level clouds (e.g., Wang et al., 2016; Mace et al., 2021), which may cause 2B-CLDCLASS-LIDAR to systematically "see" higher cloud top heights. Additionally, our studies use environmental conditions to identify MCAO conditions in order to gain insight on the types of clouds that can exist during MCAO events. Given that snowing oceanic Ns clouds tend to be thicker than Sc (Kulie et al., 2016), these Ns clouds during MCAO conditions may account for CTH > 3 km in Fig. 6. There is also evidence that snowing shallow cumuliform clouds over water can be embedded within Ns clouds (Kulie et al., 2021) and thus is another caveat to the cloud type partitioning.

Non-CAO clouds are evenly split between Sc and Ns (43 and 44% frequency, respectively; Table 1) with little inter-seasonal variability. Though this again contradicts the Kulie et al. (2016) assumption that shallow Sc snowfall events are exclusively forced by MCAO conditions, Sc snowfall rates are lower during non-CAO conditions (not shown) and may fall below the M threshold to be categorized as MCAO. The high frequency of light, shallow snowfall during non-CAO conditions motivates future research into whether reanalysis models produce similar frequency of occurrence and snowfall rate intensities for MCAO and non-CAO events. The results of this study, combined with that of Kulie et al. (2016) and Kulie & Milani (2018), indicate that not only is most CloudSat snowfall observed in the North Atlantic produced by shallow cumuliform clouds (Fig. 6, Table 1), but most North Atlantic snowfall is also associated with MCAOs (Fig. 4, 5). Furthermore, if most snowfall is produced by MCAOs, then most North Atlantic snowfall is light (< 0.1 mm h^{-1} LWE; Fig. 2).

Along the open water fetch of an MCAO, ground-based and airborne observations indicate the boundary layer deepens and shallow, mixed-phase (containing liquid and ice; Morrison et al., 2012; Korolev et al., 2017) roll clouds consequently transition to taller, glaciated, open-cellular convective clouds (e.g., Brümmer, 1999; Renfrew & Moore, 1999; Fletcher et al., 2016b; Abel et al., 2017; McCoy et al., 2017; Geerts et al., 2022). This work identified clouds as shallow Sc in regions categorized as upstream locations of MCAOs (Geerts et al., 2022), which is a notoriously difficult cloud type to parameterize in models (Field et al., 2014; Field et al., 2017; Abel et al., 2017). In the Greenland-Norwegian Seas, this cloud regime change is the result of precipitation-fueled decoupling of the boundary layer that leads to enhanced precipitation downstream (Brümmer, 1997; Abel et al., 2017) until eventually ceasing, as evidenced in the downstream regions of Fig. 3. Though not phase-specific, about 75% of the evaporated water vapor is precipitated out along the fetch of a MCAO (Brümmer, 1997; Papritz & Sodemann, 2018). This work shows that CloudSat could potentially identify these ubiquitous cloud regimes associated with MCAO snowfall events, whereas models may struggle to properly simulate stratiform clouds (Tomassini et al., 2017; Fletcher et al., 2016b; Field et al., 2017). Additionally, CloudSat captures the MCAO cloud and snowfall characteristics in a region that has very limited *in situ* observations of MCAO stratiform cloud layers (Abel et al., 2017). CloudSat, with its frequent sampling at higher latitudes, has the potential to be a useful tool to link spaceborne-derived cloud properties with surface-cloud-precipitation processes associated with MCAOs.

Analyzing MCAOs with CloudSat products gives broad but important context for satellite retrievals of snowfall. For example, the Global Precipitation Measurement (GPM) satellite employs the Goddard Profiling (GPROF) algorithm, which relies on passive microwave observations and auxiliary T2M and TCWV to constrain retrieved surface precipitation rates (Kummerow et al., 2015; Randel et al., 2020). At first-launch of the GPM satellite in 2014 (Hou et al., 2014), GPROF utilized a reference dataset that included CloudSat snowfall retrievals, meanwhile populating the database of GPM radar and radiometer observations for the succeeding, fully parametric version of GPROF (Kummerow et al., 2015). Therefore, we expect that the initial *a priori* database used by GPROF included instances of MCAO-forced snowfall observed by CloudSat. These findings therefore raise a key question of whether the current version of the GPROF *a priori* database (Randel et al., 2020) sufficiently represents MCAO snowfall events. The Dual-Frequency Precipitation Radar (DPR) on GPM operates at lower frequencies than the CPR, uses non-uniform beam filling, and has a larger footprint than the CPR (Tanelli et al. 2012), making DPR less sensitive to light, shallow snowfall (Kulie & Bennartz, 2009; Casella et al., 2017; Skofronick-Jackson et al., 2019; Silber et al. 2021; Matrosov et al., 2022). Therefore, DPR may detect MCAOs with more intense snowfall rates, but may miss lighter and/or shallow snowfall due to the limitations of the radar. Furthermore, the high frequency of MCAO conditions north of GPM's 65°N latitudinal extent would be completely missed. We see here that the distinct relationship of TCWV and T2M can inform the presence of MCAO conditions, which could assist in optimizing precipitation estimates for satellite retrievals. Future work aims to formalize the relationship between relevant environmental factors and MCAO or non-CAO snowfall events to optimize radar and radiometer retrievals.

4.1 Connection to COMBLE

The Greenland-Norwegian and Barents Seas, east of Greenland, experience the highest frequency of MCAO conditions per ERA5, especially in DJF and MAM (red box outlined in Fig. 1a). MCAOs here are responsible for severe weather impacting the UK and Norway (Brümmer, 1997; Abel et al., 2017; Papritz & Spengler 2017) making this a popular region for field experiments due to the strength, persistence, and frequency of the MCAOs (Fletcher et al., 2016a; Geerts et al., 2022). The recently completed COMBLE field campaign (Geerts et al., 2022) analyzed cloud and snowfall characteristics of three MCAO case studies that were initiated out of the Fram Strait during 2019-2020. Decades earlier, the ARKTIS 1991 and ARKTIS 1993 field campaigns used flight-track measurements to characterize MCAO case studies in this region as well (Brümmer, 1992; Brümmer, 1996). Papritz & Grams (2018) found a correlation between MCAO occurrence in these seas and the Greenland Blocking Index (Hanna et al., 2016). In Figure 8, we focus on the Greenland-Norwegian and Barents Seas and examine the two most active MCAO seasons: DJF and MAM. The window we examine here is an approximation of the region that COMBLE took place: the northeastern-most corner of our window, 60 to 82°N and -25 to 40° E (red box in Fig. 1a). The 2CSNOW rate (Fig. 8a, e) in this window is high (> 0.05 mm h^{-1}) in the northern part of the window (near the Greenland and Barents Seas), where the snowing MCAO frequency ($f_{0.01}$) is highest (Fig. 8b, f). These open-water locations are proximal to sea ice and cold continental air, making them preferential

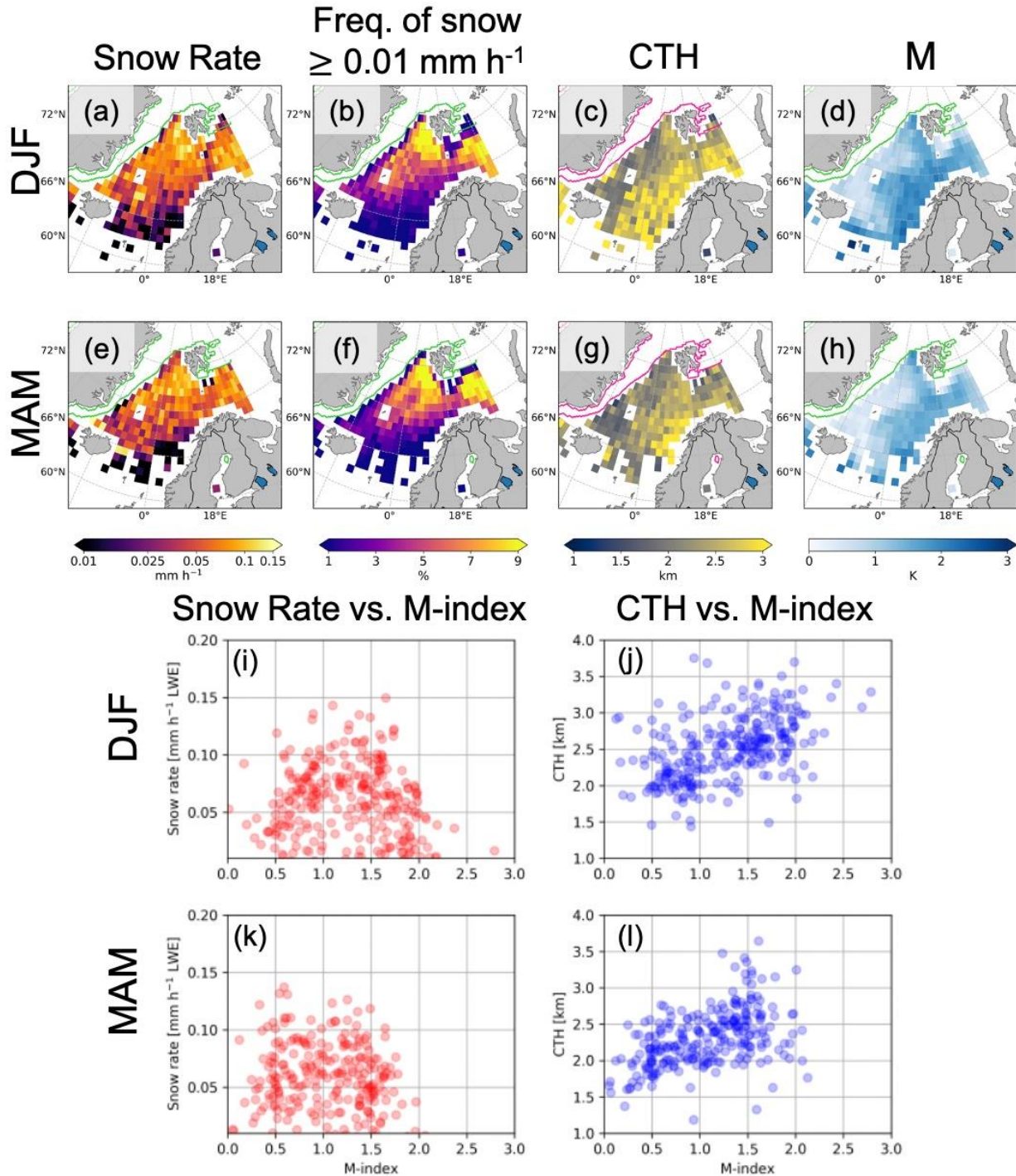pathways for an MCAO to occur in the Northern Hemisphere (Fletcher et al., 2016a; Papritz & Spengler, 2017).

Fig. 8: CloudSat 2CSNOW rates (left column), frequency of snowfall (≥ 0.01 mm h^{-1} LWE; second column), cloud-top height (CTH, third column), and M ($\theta_{SST} - \theta_{850}$, final column) in DJF (top row) and MAM (bottom row) during MCAO conditions. Snowfall (2CSNOW) rates are from 2C-SNOW-PROFILE and CTH are derived from CloudSat's 2B-CLDCLASS-LIDAR. The green line in columns 1, 2, and 4 and pink line in column 3 indicate seasonal mean sea ice extent

from ERA5. Fig. 8 i-l show mean snowfall rate vs. M-index (Fig. 8i, k) and mean CTH vs. M-index (Fig. 8j, l) for DJF (third row) and MAM (fourth row). Green line shows line of best fit through data. Snowfall (2CSNOW) rates are from 2C-SNOW-PROFILE and CTH are derived from CloudSat's 2B-CLDCLASS-LIDAR.

The CloudSat-derived seasonal mean CTH (Fig. 8c, g) show precipitating clouds are shallow (< 2 km) nearest the MCAO initiation locations but are deeper (> 2 km) further from the cold air source. Past work found that precipitation intensifies as the boundary layer deepens in the downstream region of MCAOs, which in turn acts to decouple the boundary layer (Brümmer, 1997; Abel et al., 2017). Here, higher mean snowfall rates are not necessarily observed by CloudSat. This could be the result of this work considering MCAO conditions based on temporal means within a gridbox and not the evolution of MCAO events upstream or downstream. Additionally, this work focuses solely on snowfall (and excluding rain products) from CloudSat to understand the link between MCAOs and snowfall detected by CloudSat. That is to say, there could be rain or mixed-phase precipitation further from the sea ice that enhances total precipitation rates, but the 2C-SNOW-PROFILE product (as described in Section 2) deliberately filters out liquid and mixed-phase precipitation. Plots in the fourth column show seasonal mean M indices (θ_{SST} - θ_{850}; Fig. 8d, h), and scatter plots illustrate the relationships between the M-index and snowfall rate (Fig. 8i, k) or CTH (Fig. 8j, l) in this smaller region. Here, there are signals that two MCAO cloud modes (first identified by Geerts et al., 2022) may be present: (a) higher CTH coincident with larger values of M (closer to the Norwegian coast, and (b) lower CTH coincident with lower values of M (near the sources of cold air). Higher values of M further from the sea ice may also reflect a deeper boundary layer that accompanies higher CTH. Importantly, the M values here are calculated from ERA5 while CTH is derived from CloudSat and are therefore completely separate pieces of information consistent with the transition between two distinct cloud modes during MCAOs as described in previous studies. Closer to the Norwegian coast, CloudSat snowfall is less frequent (Fig. 8b, f), and produced from clouds with higher CTH (Fig. 8c, g) paired with larger M-indices (Fig. 8d, h, j, l), indicating that cold-air outbreaks must be of greater strength to initiate snowfall with increased distance from cold air sources. It is also possible that along the fetch of MCAOs, precipitation phase change occurs and while total precipitation rates (rain, snow, mixed) may be heavy as found in Geerts et al. (2022), Fig. 8a, e, i, k do not show discernable difference in mean snowfall rates with increasing M-index values. Future work will include wind data to investigate the fetch-dependency of precipitation phase, as this study focuses only on how the prevalent snowfall that CloudSat can detect is connected to MCAOs.

Figure 9 shows seasonal mean and anomalous (deviations from the mean) SSTs (Fig. 9a), T2M (Fig. 9b), T_{850} (Fig. 9c), and TCWV (Fig. 9d) from the ERA5 dataset in DJF (rows 1 and 2) and MAM (rows 3 and 4) during snowing (2CSNOW > 0) MCAO conditions. Mean SST (T2M) is often above (near) freezing for both seasons, with anomalously lower T2M that coincides with the regions of high MCAO frequency, $f_{0.01}$ (as shown in Fig. 8b, f) near the mean sea ice boundary. Differences between SST and T2M can inform on the magnitude of ocean-to-atmosphere heat fluxes but is not a good identifier for MCAOs (McCoy et al., 2017). At 850 hPa, negative anomalies of T_{850} are even larger in magnitude and extend a greater distance from the mean sea ice edge. Seasonal mean TCWV is generally < 6 mm in this region for both DJF and

MAM, representing the dry conditions often associated with cold temperatures. Notably, coincident with the highest T_{850} anomalies are the largest TCWV dry anomalies, informing that while the environment near sea ice may be anomalously cold and dry, MCAO conditions will still produce snowfall due to the convective interaction with the relatively warm, open ocean water.
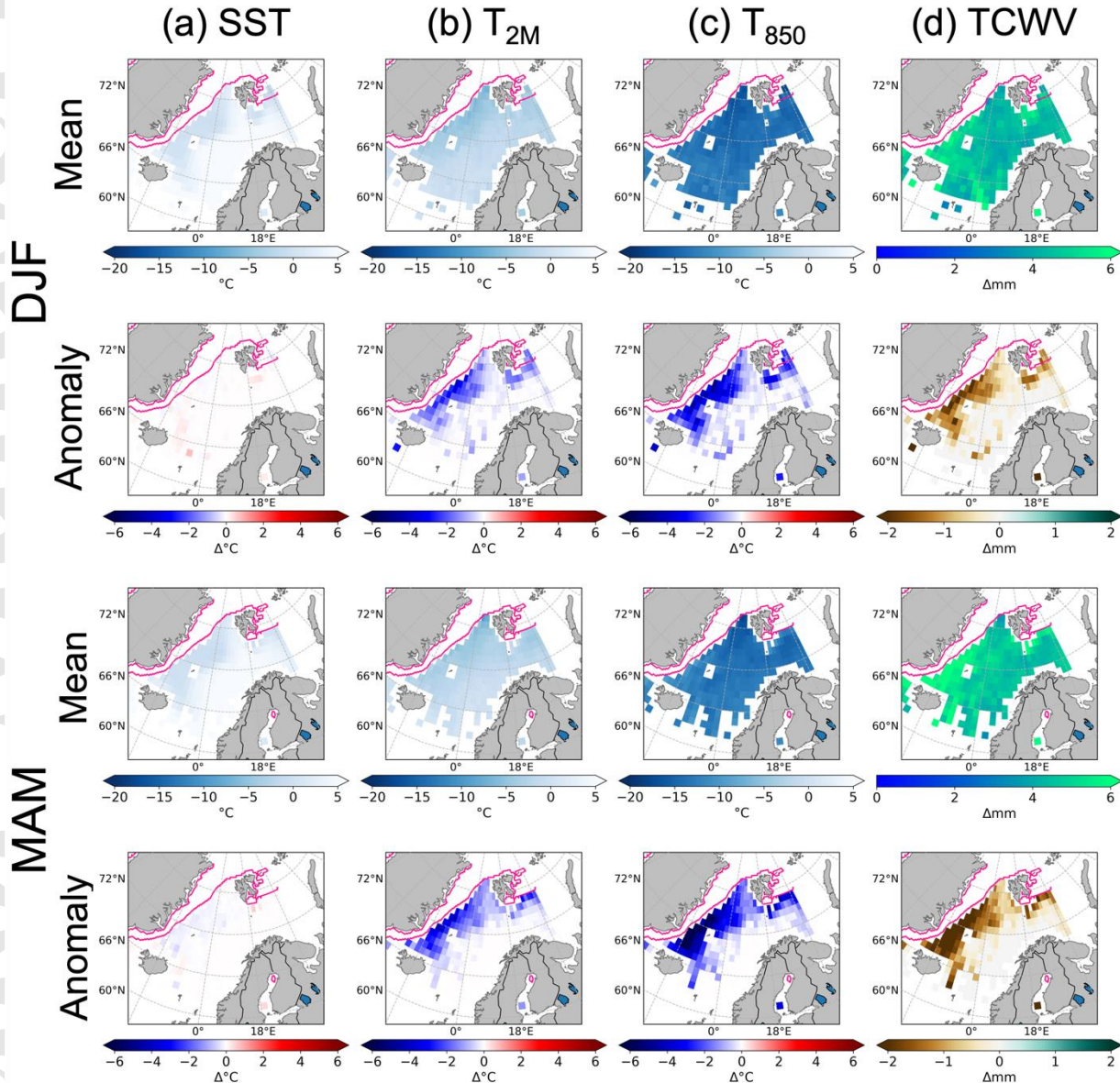

Fig. 9: Mean and anomalous (deviations from the mean) ERA5 sea surface temperature (SST, 9a), two-meter temperature (T2M, 9b), 850 hPa temperature (T_{850}, 9c), and total column water vapor (TCWV, 9d) during snowing MCAO conditions, 2CSNOW > 0. The top (bottom) two rows are DJF (MAM).

From this meteorological analysis, we see that North Atlantic MCAOs in this window are initiated by cold air originating over sea ice or land and advecting over relatively warm and open water surfaces in the Greenland-Norwegian and Barents Seas (Fig. 9a-c). Negative T_{850} and TCWV anomalies (Fig. 9c, d) over water force intense sensible and latent heat loss from the surface (Brümmer, 1999; Renfrew & Moore, 1999), leading to the formation of shallow (< 2 km) stratocumulus clouds in regions closer to sea ice (Fig. 8c, g and Table 1). Snowfall during MCAOs is most frequent in the Fram Strait and Barents Sea (Fig. 8b, f) and is associated with high snowfall rates (> 0.05 mm h^{-1}; Fig. 8a, e). CTH is higher toward the southeast (4-5 km; Fig. 8c, g) indicative of a deeper boundary layer. M values also increase from just above 0 near the sea ice edge to ~2-3 at the far southern reaches of the domain. Despite CTH and M being derived from two independent datasets (CloudSat and ERA5, respectively), we see a remarkably similar spatial pattern in increasing M and CTH in the downstream direction that illustrates the transition of MCAO cloud modes associated with fetch (Geerts et al., 2022).

The downstream region of MCAOs is near Norway and Russia, where enhanced precipitation should force clouds to transition to an open-cellular convection pattern (Abel et al., 2017; McCoy et al., 2017). Here, we show higher CTH (Fig. 8c, g) and have previously identified most (~75%) MCAO clouds as Sc (Table 1). Snowfall rates do not necessarily increase with fetch (Fig. 8a, e), potentially due to a precipitation phase transition that would reduce 2CSNOW rates but increase rain rates. Another hypothesis is that the seemingly scattered pattern of snowfall rates in the downstream regions are representative of the stratiform open-cellular convection found here during MCAOs (Abel et al., 2017; Geerts et al., 2022) that becomes more disorganized moving equatorward (McCoy et al., 2017). These results from CloudSat reflect underlying physical mechanisms responsible for development and apparent fetch-dependent decay of snowfall rates, whether these are phase transitions, organized linear to open cellular convection evolution, decoupling of the boundary layer from the surface due to precipitation, or other effects. Future work will examine where precipitation phase occurs along the fetch of MCAOs using satellite observations.

5 Conclusion

In this work, we combined CloudSat satellite observations of snowfall and clouds with an ERA5-derived M index (M $\equiv \theta_{SST} - \theta_{850} > 0$) and reanalysis data products to analyze the frequency and meteorological impact of MCAOs in the North Atlantic Ocean. In the North Atlantic, the highest frequency of MCAO conditions occurs in boreal wintertime (DJF), followed by spring (MAM), autumn (SON), and summer (JJA, not included in this study due to infrequency of MCAO conditions and CloudSat snowfall). Ocean regions nearest cold continental land and sea ice experience the highest frequency of MCAO conditions: the Greenland Sea, Barents Sea, Norwegian Sea, Labrador Sea, and Baffin Bay. Sea ice extent ($\geq 50\%$ concentration) is highest in MAM, followed by DJF, then SON.

CloudSat snowfall observations in the North Atlantic are often associated with MCAO conditions. The most active seasons in terms of collocated CloudSat snowfall and MCAO frequency are DJF, MAM, and SON, respectively. Spatial distributions of CloudSat snowfall show higher mean rates associated with areas of high frequency of MCAO conditions, particularly in the Barents, Greenland, and Labrador Seas. In SON, open waters in the Baffin

Bay experience enhanced snowfall rates. Non-CAO snowfall rates are generally much lower except along mean sea ice edge. We hypothesize that enhanced rates in the Baffin Bay during non-CAO conditions in SON may be related to atmospheric blocking patterns, to be further investigated in future work. When filtering frequency of MCAO conditions by CloudSat snowfall occurrence, the Barents and Greenland Seas experience the highest frequency throughout the year, followed by the Norwegian Sea. CloudSat observes snowfall less frequently during non-CAO conditions year-round.

During MCAO conditions, cloud top heights tend to be lower (< 3 km) except in downstream regions where boundary layer growth is associated with higher cloud tops. The M index is larger in magnitude further from cold air sources, confirming via independent datasets (CloudSat and ERA5) the relationship between larger M indices and taller CTH that is consistent with the presence of two distinct modes, as identified during the COMBLE field campaign (Geerts et al., 2022). Stratocumulus clouds are the most prevalent in the North Atlantic, making up 76% (44%) of snowing clouds identified during MCAO (non-CAO) conditions. The remaining cloud types identified are mostly nimbostratus clouds: 18% during MCAO conditions and 43% during non-CAO conditions. Snow produced by stratocumulus clouds that are embedded within deeper nimbostratus cloud structures are also difficult for the 2B-CLDCLASS-LIDAR to isolate as a unique category. Such instances are typically classified as nimbostratus events, but this classification does not reflect important process-related features indicated by the shallow embedded convective features. These complex, multi-scale cloud processes familiar to MCAOs are difficult for general circulation models to capture (Tomassini et al., 2017; de Roode et al., 2019) and are therefore better suited to be studied by direct observations. Our work shows that CloudSat retrievals provide valuable, detailed information to study cloud and precipitation during MCAOs in remote, high-latitude locations. Additionally, our work suggests that future satellite missions that include radar and/or lidar onboard will contribute to the collection of satellite data assimilated into reanalysis datasets to further address the "grey zone" problem. Follow-on studies will further analyze whether CloudSat can capture the evolution of clouds and precipitation during MCAO events and incorporate additional satellite data products.

Open Research

The CloudSat 2C-SNOW-PROFILE (https://www.cloudsat.cira.colostate.edu/data-products/2c-snow-profile) and 2B-CLDCLASS-LIDAR (https://www.cloudsat.cira.colostate.edu/data-products/2b-cldclass-lidar) data products were downloaded from the CloudSat Data Processing Center. Hourly ERA5 reanalysis data (Hersbach et al., 2020) was downloaded from the Copernicus Climate Data Store (CDS).

References

Abel, S. J., Boutle, I. A., Waite, K., Fox, S., Brown, P. R., Cotton, R., et al. (2017). The role of precipitation in controlling the transition from stratocumulus to cumulus clouds in a Northern Hemisphere cold-air outbreak. *Journal of the Atmospheric Sciences*, *74*(7), 2293-2314. https://doi.org/10.1175/JAS-D-16-0362.1

Afargan-Gerstman, H., Polkova, I., Papritz, L., Ruggieri, P., King, M. P., Athanasiadis, P. J., et al. (2020). Stratospheric influence on North Atlantic marine cold air outbreaks following sudden stratospheric warming events. *Weather and Climate Dynamics*, *1*(2), 541-553. https://doi.org/10.5194/wcd-1-541-2020

Battaglia, A., Haynes, J. M., L'Ecuyer, T., & Simmer, C. (2008). Identifying multiple-scattering-affected profiles in CloudSat observations over the oceans. *Journal of Geophysical Research: Atmospheres*, *113*(D8). https://doi.org/10.1029/2008JD009960

Battaglia, A., & Delanoë, J. (2013). Synergies and complementarities of CloudSat-CALIPSO snow observations. *Journal of Geophysical Research: Atmospheres*, *118*(2), 721-731. https://doi.org/10.1029/2012JD018092

Battaglia, A., & Panegrossi, G. (2020). What can we learn from the CloudSat radiometric mode observations of snowfall over the ice-free ocean? *Remote Sensing*, *12*(20), 3285. https://doi.org/10.3390/rs12203285

Bennartz, R., Fell, F., Pettersen, C., Shupe, M. D., & Schuettemeyer, D. (2019). Spatial and temporal variability of snowfall over Greenland from CloudSat observations. *Atmospheric Chemistry and Physics*, *19*(12), 8101-8121. https://doi.org/10.5194/acp-19-8101-2019

Brümmer, B. (1992). ARKTIS 1991. Report on the field phase with examples of measurements.

Brümmer, B. (1996). Boundary-layer modification in wintertime cold-air outbreaks from the Arctic sea ice. *Boundary-Layer Meteorology*, *80*(1), 109-125. https://doi.org/10.1007/BF00119014

Brümmer, B. (1997). Boundary Layer Mass, Water, and Heat Budgets in Wintertime Cold-Air Outbreaks from the Arctic Sea Ice. *Monthly Weather Review*, *125(8)*, 1824-1837. https://doi.org/10.1175/1520-0493(1997)125<1824:BLMWAH>2.0.CO;2

Brümmer, B. (1999). Roll and cell convection in wintertime Arctic cold-air outbreaks. *Journal of the atmospheric sciences*, *56*(15), 2613-2636. https://doi.org/10.1175/1520-0469(1999)056<2613:RACCIW>2.0.CO;2

Cao, Q., Hong, Y., Chen, S., Gourley, J. J., Zhang, J., & Kirstetter, P. E. (2014). Snowfall detectability of NASA's cloudsat: The first cross-investigation of its 2C-snow-profile product and national multi-sensor mosaic QPE (NMQ) snowfall data. *Progress in electromagnetics research*, *148*, 55-61. https://doi.org/10.2528/PIER14030405

Casella, D., Panegrossi, G., Sanò, P., Marra, A. C., Dietrich, S., Johnson, B. T., et al. (2017). Evaluation of the GPM-DPR snowfall detection capability: Comparison with CloudSat-CPR. *Atmospheric Research*, *197*, 64-75. https://doi.org/10.1016/j.atmosres.2017.06.018

Chase, R. J., Nesbitt, S. W., McFarquhar, G. M., Wood, N. B., & Heymsfield, G. M. (2022). Direct comparisons between GPM-DPR and CloudSat snowfall retrievals. *Journal of Applied Meteorology and Climatology*, *61*(9), 1257-1271. https://doi.org/10.1175/JAMC-D-21-0081.1

Chen, S., Hong, Y., Kulie, M., Behrangi, A., Stepanian, P. M., Cao, Q., ... & Zhang, X. (2016). Comparison of snowfall estimates from the NASA CloudSat cloud profiling radar and NOAA/NSSL multi-radar multi-sensor system. *Journal of Hydrology*, *541*, 862-872. https://doi.org/10.1016/j.jhydrol.2016.07.047

Dickson, R., Lazier, J., Meincke, J., Rhines, P., & Swift, J. (1996). Long-term coordinated changes in the convective activity of the North Atlantic. Progress in Oceanography, 38(3), 241-295. https://doi.org/10.1016/S0079-6611(97)00002-5

Durden, S. L., Tanelli, S., & Dobrowalski, G. (2010). CloudSat W-band radar measurements of surface backscatter. *IEEE Geoscience and Remote Sensing Letters*, *8*(3), 401-405. https://doi.org/10.1109/LGRS.2010.2079314

de Roode, S. R., Frederikse, T., Siebesma, A. P., Ackerman, A. S., Chylik, J., Field, P. R., ... & Tomassini, L. (2019). Turbulent transport in the gray zone: A large eddy model intercomparison study of the CONSTRAIN cold air outbreak case. Journal of Advances in Modeling Earth Systems, 11(3), 597-623. https://doi.org/10.1029/2018MS001443

Field, P. R., Cotton, R. J., McBeath, K., Lock, A. P., Webster, S., & Allan, R. P. (2014). Improving a convection-permitting model simulation of a cold air outbreak. *Quarterly Journal of the Royal Meteorological Society*, *140*(678), 124-138. https://doi.org/10.1002/qj.2116

Field, P. R., Brožková, R., Chen, M., Dudhia, J., Lac, C., Hara, T., et al. (2017). Exploring the convective grey zone with regional simulations of a cold air outbreak. *Quarterly Journal of the Royal Meteorological Society*, *143*(707), 2537-2555. https://doi.org/10.1002/qj.3105.

Fletcher, J., Mason, S., & Jakob, C. (2016a). The climatology, meteorology, and boundary layer structure of marine cold air outbreaks in both hemispheres. *Journal of Climate*, *29*(6), 1999-2014. https://doi.org/10.1175/JCLI-D-15-0268.1

Fletcher, J. K., Mason, S., & Jakob, C. (2016b). A climatology of clouds in marine cold air outbreaks in both hemispheres. *Journal of Climate*, *29*(18), 6677-6692. https://doi.org/10.1175/JCLI-D-15-0783.1

Geerts, B., Giangrande, S. E., McFarquhar, G. M., Xue, L., Abel, S. J., Comstock, J. M., et al. (2022). The COMBLE campaign: a study of marine boundary-layer clouds in Arctic cold-air

outbreaks. *Bulletin of the American Meteorological Society*. https://doi.org/10.1175/BAMS-D-21-0044.1

Gryschka, M., Witha, B., & Etling, D. (2008). Scale analysis of convective clouds. *Meteorologische Zeitschrift*, *17*(6), 785. https://doi.org/10.1127/0941-2948/2008/0345

Hanna, E., Cropper, T. E., Hall, R. J., & Cappelen, J. (2016). Greenland Blocking Index 1851–2015: a regional climate change signal. *International Journal of Climatology*, *36*(15), 4847-4861. https://doi.org/10.1002/joc.4673

Hartmann, J., Kottmeier, C., & Raasch, S. (1997). Roll vortices and boundary-layer development during a cold air outbreak. *Boundary-Layer Meteorology*, *84*(1), 45-65. https://doi.org/10.1023/A:1000392931768.

Hersbach, H., Bell, B., Berrisford, P., Hirahara, S., Horányi, A., Muñoz-Sabater, J., et al. (2020). The ERA5 global reanalysis. *Quarterly Journal of the Royal Meteorological Society*, *146*(730), 1999-2049, doi: 10.1002/qj.3803

Hiley, M. J., Kulie, M. S., & Bennartz, R. (2011). Uncertainty analysis for CloudSat snowfall retrievals. *Journal of Applied Meteorology and Climatology*, *50*(2), 399-418. https://doi.org/10.1175/2010JAMC2505.1

Hou, A. Y., Kakar, R. K., Neeck, S., Azarbarzin, A. A., Kummerow, C. D., Kojima, M., et al. (2014). The global precipitation measurement mission. *Bulletin of the American meteorological Society*, *95*(5), 701-722. https://doi.org/10.1175/BAMS-D-13-00164.1

Haynes, J. M., L'Ecuyer, T. S., Stephens, G. L., Miller, S. D., Mitrescu, C., Wood, N. B., & Tanelli, S. (2009). Rainfall retrieval over the ocean with spaceborne W-band radar. Journal of Geophysical Research: Atmospheres, 114(D8). https://doi.org/10.1029/2008JD009973

Im, E., Wu, C., & Durden, S. L. (2005). Cloud profiling radar for the CloudSat mission. In *IEEE International Radar Conference, 2005,* 483-486. 10.1109/RADAR.2005.1435874

Kodamana, R., & Fletcher, C. G. (2021). Validation of CloudSat-CPR derived precipitation occurrence and phase estimates across Canada. *Atmosphere*, *12*(3), 295. https://doi.org/10.3390/atmos12030295

Kolstad, E. W., Bracegirdle, T. J., & Seierstad, I. A. (2009). Marine cold-air outbreaks in the North Atlantic: Temporal distribution and associations with large-scale atmospheric circulation. *Climate dynamics*, *33*(2), 187-197. https://doi.org/10.1007/s00382-008-0431-5

Korolev, A., McFarquhar, G., Field, P. R., Franklin, C., Lawson, P., Wang, Z., et al. (2017). Mixed-phase clouds: Progress and challenges. *Meteorological Monographs*, *58*, 5-1. https://doi.org/10.1175/AMSMONOGRAPHS-D-17-0001.1

Kulie, M. S., & Bennartz, R. (2009). Utilizing spaceborne radars to retrieve dry snowfall. *Journal of Applied Meteorology and Climatology*, *48*(12), 2564-2580. https://doi.org/10.1175/2009JAMC2193.1

Kulie, M. S., & Milani, L. (2018). Seasonal variability of shallow cumuliform snowfall: A CloudSat perspective. *Quarterly Journal of the Royal Meteorological Society*, *144*, 329-343. https://doi.org/10.1002/qj.3222

Kulie, M. S., Milani, L., Wood, N. B., Tushaus, S. A., Bennartz, R., & L'Ecuyer, T. S. (2016). A shallow cumuliform snowfall census using spaceborne radar. *Journal of Hydrometeorology*, *17*(4), 1261-1279. https://doi.org/10.1175/JHM-D-15-0123.1

Kulie, M. S., Pettersen, C., Merrelli, A. J., Wagner, T. J., Wood, N. B., Dutter, M., ... & Petersen, W. A. (2021). Snowfall in the Northern Great Lakes: lessons learned from a multisensor observatory. Bulletin of the American Meteorological Society, 102(7), E1317-E1339. https://doi.org/10.1175/BAMS-D-19-0128.1

Kummerow, C. D., Randel, D. L., Kulie, M., Wang, N., Ferraro, R., Joseph Munchak, S., & Petkovic, V. (2015). The Evolution of the Goddard Profiling Algorithm to a Fully Parametric Scheme, *Journal of Atmospheric and Oceanic Technology*, *32*(12), 2265-2280. https://doi.org/10.1175/JTECH-D-15-0039.1

Landgren, O. A., Seierstad, I. A., & Iversen, T. (2019). Projected future changes in Marine Cold-Air Outbreaks associated with polar lows in the Northern North-Atlantic Ocean. *Climate Dynamics*, *53*(5), 2573-2585. https://doi.org/ 10.1007/s00382-019-04642-2

Liu, G. (2008). Deriving snow cloud characteristics from CloudSat observations. *Journal of Geophysical Research: Atmospheres*, *113*(D8). https://doi.org/10.1029/2007JD009766

Maahn, M., Burgard, C., Crewell, S., Gorodetskaya, I. V., Kneifel, S., Lhermitte, S., et al. (2014). How does the spaceborne radar blind zone affect derived surface snowfall statistics in polar regions?. *Journal of Geophysical Research: Atmospheres*, *119*(24), 13-604. https://doi.org/10.1002/2014JD022079

Mace, G. G., Protat, A., & Benson, S. (2021). Mixed-Phase Clouds Over the Southern Ocean as Observed From Satellite and Surface Based Lidar and Radar. *Journal of Geophysical Research: Atmospheres*, *126*(16), e2021JD034569. https://doi.org/10.1029/2021JD034569

Matrosov, S. Y. (2007). Modeling backscatter properties of snowfall at millimeter wavelengths. *Journal of the atmospheric sciences*, *64*(5), 1727-1736. https://doi.org/10.1175/JAS3904.1

Matrosov, S. Y., Shupe, M. D., & Uttal, T. (2022). High temporal resolution estimates of Arctic snowfall rates emphasizing gauge and radar-based retrievals from the MOSAiC expedition. *Elem Sci Anth*, *10*(1), 00101. https://doi.org/10.1525/elementa.2021.00101

McErlich, C., McDonald, A., Schuddeboom, A., & Silber, I. (2021). Comparing Satellite-and Ground-Based Observations of Cloud Occurrence Over High Southern Latitudes. *Journal of Geophysical Research: Atmospheres*, *126*(6), e2020JD033607. https://doi.org/10.1029/2020JD033607

McIlhattan, E. A., L'Ecuyer, T. S., & Miller, N. B. (2017). Observational evidence linking Arctic supercooled liquid cloud biases in CESM to snowfall processes. *Journal of Climate*, *30*(12), 4477-4495. https://doi.org/10.1175/JCLI-D-16-0666.1

McIlhattan, E. A., Pettersen, C., Wood, N. B., & L'Ecuyer, T. S. (2020). Satellite observations of snowfall regimes over the Greenland Ice Sheet. *The Cryosphere*, *14*(12), 4379-4404. https://doi.org/10.5194/tc-14-4379-2020

Milani, L., & Wood, N. B. (2021). Biases in CloudSat falling snow estimates resulting from daylight-only operations. *Remote Sensing*, *13*(11), 2041. https://doi.org/10.3390/rs13112041

McCoy, I. L., Wood, R., & Fletcher, J. K. (2017). Identifying meteorological controls on open and closed mesoscale cellular convection associated with marine cold air outbreaks. Journal of Geophysical Research: Atmospheres, 122, 11,678–11,702. https://doi.org/10.1002/2017JD027031

Morrison, H., De Boer, G., Feingold, G., Harrington, J., Shupe, M. D., & Sulia, K. (2012). Resilience of persistent Arctic mixed-phase clouds. *Nature Geoscience*, *5*(1), 11-17. https://doi.org/10.1038/ngeo1332

Norin, L., Devasthale, A., L'Ecuyer, T. S., Wood, N. B., & Smalley, M. (2015). Intercomparison of snowfall estimates derived from the CloudSat Cloud Profiling Radar and the ground-based weather radar network over Sweden. *Atmos. Meas. Tech.*, *8*, 5009–5021. https://doi.org/10.5194/amt-8-5009-2015

Palerme, C., Claud, C., Dufour, A., Genthon, C., Wood, N. B., & L'Ecuyer, T. (2017). Evaluation of Antarctic snowfall in global meteorological reanalyses. *Atmospheric Research*, *190*, 104-112. https://doi.org/10.1016/j.atmosres.2017.02.015

Palerme, C., Kay, J. E., Genthon, C., L'Ecuyer, T., Wood, N. B., & Claud, C. (2014). How much snow falls on the Antarctic ice sheet?. *The Cryosphere*, *8*(4), 1577-1587. https://doi.org/10.5194/tc-8-1577-2014

Papritz, L., & Grams, C. M. (2018). Linking low-frequency large-scale circulation patterns to cold air outbreak formation in the northeastern North Atlantic. *Geophysical Research Letters*, *45*(5), 2542-2553. https://doi.org/10.1002/2017GL076921

Papritz, L., & Spengler, T. (2017). A Lagrangian climatology of wintertime cold air outbreaks in the Irminger and Nordic Seas and their role in shaping air–sea heat fluxes. *Journal of Climate*, *30*(8), 2717-2737. https://doi.org/10.1175/JCLI-D-16-0605.1

Papritz, L., & Sodemann, H. (2018). Characterizing the local and intense water cycle during a cold air outbreak in the Nordic seas. *Monthly Weather Review*, *146*(11), 3567-3588. https://doi.org/10.1175/MWR-D-18-0172.1

Papritz, L., Pfahl, S., Sodemann, H., & Wernli, H. (2015). A climatology of cold air outbreaks and their impact on air–sea heat fluxes in the high-latitude South Pacific. Journal of Climate, 28(1), 342-364. https://doi.org/10.1175/JCLI-D-14-00482.1

Pettersen, C., Henderson, S. A., Mattingly, K. S., Bennartz, R., & Breeden, M. L. (2022). The Critical Role of Euro-Atlantic Blocking in Promoting Snowfall in Central Greenland. *Journal of Geophysical Research: Atmospheres*, *127*(6), e2021JD035776. https://doi.org/10.1029/2021JD035776

Randel, D. L., Kummerow, C. D., & Ringerud, S. (2020). The Goddard Profiling (GPROF) precipitation retrieval algorithm. In *Satellite precipitation measurement* (pp. 141-152). Springer, Cham.

Rasmussen, E.A., and J. Turner, 2003: Polar Lows: Mesoscale Weather Systems in the Polar Regions. Cambridge University Press, 612 pp.

Renfrew, I. A., & Moore, G. W. K. (1999). An extreme cold-air outbreak over the Labrador Sea: Roll vortices and air–sea interaction. *Monthly Weather Review*, *127*(10), 2379-2394. https://doi.org/10.1175/1520-0493(1999)127<2379:AECAOO>2.0.CO;2

Sanchez, K. J., Zhang, B., Liu, H., Brown, M. D., Crosbie, E. C., Gallo, F., et al. (2022). North Atlantic Ocean SST-gradient-driven variations in aerosol and cloud evolution along Lagrangian cold-air outbreak trajectories. *Atmospheric Chemistry and Physics*, *22*(4), 2795-2815. https://doi.org/10.5194/acp-22-2795-2022

Sassen, K., & Wang, Z. (2008). Classifying clouds around the globe with the CloudSat radar: 1-year of results. *Geophysical research letters*, *35*(4). https://doi.org/10.1029/2008JD009972

Shapiro, M. A., Fedor, L. S., & Hampel, T. (1987). Research aircraft measurements of a polar low over the Norwegian Sea. *Tellus A: Dynamic Meteorology and Oceanography*, *39*(4), 272-306. https://doi.org/10.3402/tellusa.v39i4.11761

Shates, J. A., Pettersen, C., L'Ecuyer, T. S., & Kulie, M. S. (2023). Multi-year analysis of rain-snow levels at Marquette, Michigan. Journal of Geophysical Research: Atmospheres, e2022JD037132. https://doi.org/10.1029/2022JD037132

Silber, I., Fridlind, A. M., Verlinde, J., Ackerman, A. S., Cesana, G. V., & Knopf, D. A. (2021). The prevalence of precipitation from polar supercooled clouds. *Atmospheric Chemistry and Physics*, *21*(5), 3949-3971. https://doi.org/10.5194/acp-21-3949-2021

Skofronick-Jackson, G., Kulie, M., Milani, L., Munchak, S. J., Wood, N. B., & Levizzani, V. (2019). Satellite estimation of falling snow: A global precipitation measurement (GPM) core observatory perspective. *Journal of applied meteorology and climatology*, *58*(7), 1429-1448. https://doi.org/10.1175/JAMC-D-18-0124.1

Smith, E. T., & Sheridan, S. C. (2020). Where do cold air outbreaks occur, and how have they changed over time? *Geophysical Research Letters*, *47*(13), e2020GL086983. https://doi.org/10.1029/2020GL086983

Smith, E. T., & Sheridan, S. C. (2021). The relationship between teleconnections, surface temperature, and cold air outbreaks. *International Journal of Climatology*, *42*(3), 1531-1543. https://doi.org/10.1002/joc.7318

Souverijns, N., Gossart, A., Gorodetskaya, I. V., Lhermitte, S., Mangold, A., Laffineur, Q., et al. (2018). How does the ice sheet surface mass balance relate to snowfall? Insights from a ground-based precipitation radar in East Antarctica. *The Cryosphere*, *12*(6), 1987-2003. https://doi.org/10.5194/tc-12-1987-2018

Stephens, G. L., Vane, D. G., Boain, R. J., Mace, G. G., Sassen, K., Wang, Z., et al. (2002). The CloudSat mission and the A-Train: A new dimension of space-based observations of clouds and precipitation. *Bulletin of the American Meteorological Society*, *83*(12), 1771-1790. https://doi.org/10.1175/BAMS-83-12-1771

Stephens, G. L., Vane, D. G., Tanelli, S., Im, E., Durden, S., Rokey, M., et al. (2008). CloudSat mission: Performance and early science after the first year of operation. *Journal of Geophysical Research: Atmospheres*, *113*(D8). https://doi.org/10.1029/2008JD009982

Stephens, G., Winker, D., Pelon, J., Trepte, C., Vane, D., Yuhas, C., et al.. (2018). CloudSat and CALIPSO within the A-Train: Ten years of actively observing the Earth system. *Bulletin of the American Meteorological Society*, *99*(3), 569-581. https://doi.org/10.1175/BAMS-D-16-0324.1

Tanelli, S., Durden, S. L., Im, E., Pak, K. S., Reinke, D. G., Partain, P., et al. (2008). CloudSat's cloud profiling radar after two years in orbit: Performance, calibration, and processing. *IEEE Transactions on Geoscience and Remote Sensing*, *46*(11), 3560-3573. https://doi.org/10.1029/2008JD009982

Tanelli, S., Sacco, G. F., Durden, S. L., & Haddad, Z. S. (2012). Impact of non-uniform beam filling on spaceborne cloud and precipitation radar retrieval algorithms. *Remote Sensing of the Atmosphere, Clouds, and Precipitation IV, 8523*, 20-28. https://doi.org/10.1117/12.977375

Terpstra, A., Renfrew, I. A., and Sergeev, D. E. (2021). Characteristics of Cold-Air Outbreak Events and Associated Polar Mesoscale Cyclogenesis over the North Atlantic Region. *Journal of Climate* 34, 11, 4567-4584. https://doi.org/10.1175/JCLI-D-20-0595.1

Tomassini, L., Field, P. R., Honnert, R., Malardel, S., McTaggart-Cowan, R., Saitou, K., ... & Seifert, A. (2017). The "G rey Z one" cold air outbreak global model intercomparison: A cross evaluation using large-eddy simulations. Journal of Advances in Modeling Earth Systems, 9(1), 39-64. https://doi.org/10.1002/2016MS000822

Wang, Y., Liu, G., Seo, E. K., & Fu, Y. (2013). Liquid water in snowing clouds: Implications for satellite remote sensing of snowfall. *Atmospheric research*, *131*, 60-72. https://doi.org/10.1016/j.atmosres.2012.06.008

Wang, Z. (2019) CloudSat 2B-CLDCLASS-LIDAR product process description and interface control document. *Process Description and Interface Control Document (PDICD) P1_R05, NASA*, *33*. Available at: https://www.cloudsat.cira.colostate.edu/cloudsat-static/info/dl/2b-cldclass-lidar/2B-CLDCLASS-LIDAR_PDICD.P1_R05.rev0_.pdf (last access: 15 August 2022).

Wang, T., Fetzer, E. J., Wong, S., Kahn, B. H., & Yue, Q. (2016). Validation of MODIS cloud mask and multilayer flag using CloudSat-CALIPSO cloud profiles and a cross-reference of their cloud classifications. Journal of Geophysical Research: Atmospheres, 121(19), 11-620. https://doi.org/10.1002/2016JD025239

Wendisch, M., Macke, A., Ehrlich, A., Lüpkes, C., Mech, M., Chechin, D., et al. (2019). The Arctic cloud puzzle: Using ACLOUD/PASCAL multiplatform observations to unravel the role of clouds and aerosol particles in Arctic amplification. *Bulletin of the American Meteorological Society*, *100*(5), 841-871. https://doi.org/10.1175/BAMS-D-18-0072.1

Wendisch, M., Brückner, M., Crewell, S., Ehrlich, A., Notholt, J., Lüpkes, C., et al.(2022). Atmospheric and surface processes, and feedback mechanisms determining Arctic amplification: A review of first results and prospects of the (AC) 3 project. *Bulletin of the American Meteorological Society*. https://doi.org/10.1175/BAMS-D-21-0218.1

West, T. K., Steenburgh, W. J., & Mace, G. G. (2019). Characteristics of sea-effect clouds and precipitation over the sea of Japan region as observed by A-Train satellites. *Journal of Geophysical Research: Atmospheres*, *124*(3), 1322-1335. https://doi.org/10.1029/2018JD029586

Winker, D. M., Hunt W. H., & McGill M. J. (2007). Initial performance assessment of CALIOP. *Geophys. Res. Lett.*, *34*, L19803. 10.1029/2007GL030135

Winker, D. M., Vaughan, M. A., Omar, A., Hu, Y., Powell, K. A., Liu, Z., Hunt, W. H., & Young, S. A. (2009). Overview of the CALIPSO Mission and CALIOP Data Processing Algorithms, *Journal of Atmospheric and Oceanic Technology*, *26*(11), 2310-2323. https://doi.org/10.1175/2009JTECHA1281.1

Wood, N. B., & L'Ecuyer, T. S. *Level 2C Snow Profile Process Description and Interface Control Document, Product Version P1_R05*; NASA JPL CloudSat Project Document Revision 0; National Aeronautics and Space Administration, Jet Propulsion Laboratory: Pasadena, CA, USA, 2018; pp. 1–26. Available online: https://www.cloudsat.cira.colostate.edu/data-products/2c-snow-profile#:~:text=2C%2DSNOW%2DPROFILE%20P1_R05%20PDICD%20(Rev.%200) (last access: 15 August 2022).

Woods, C., Caballero, R., & Svensson, G. (2017). Representation of Arctic moist intrusions in CMIP5 models and implications for winter climate biases. *Journal of Climate*, *30*(11), 4083-4102. https://doi.org/10.1175/JCLI-D-16-0710.1

Wu, P., & Ovchinnikov, M. (2022). Cloud morphology evolution in Arctic cold-air outbreak: two cases during COMBLE period. *Journal of Geophysical Research: Atmospheres*, e2021JD035966. https://doi.org/10.1029/2021JD035966

Yang, Q., & Geerts, B. (2006). Horizontal convective rolls in cold air over water: Buoyancy characteristics of coherent plumes detected by an airborne radar. *Monthly weather review*, *134*(9), 2373-2396. https://doi.org/10.1175/MWR3203.1